



저작자표시-비영리-변경금지 2.0 대한민국

이용자는 아래의 조건을 따르는 경우에 한하여 자유롭게

- 이 저작물을 복제, 배포, 전송, 전시, 공연 및 방송할 수 있습니다.

다음과 같은 조건을 따라야 합니다:



저작자표시. 귀하는 원저작자를 표시하여야 합니다.



비영리. 귀하는 이 저작물을 영리 목적으로 이용할 수 없습니다.



변경금지. 귀하는 이 저작물을 개작, 변형 또는 가공할 수 없습니다.

- 귀하는, 이 저작물의 재이용이나 배포의 경우, 이 저작물에 적용된 이용허락조건을 명확하게 나타내어야 합니다.
- 저작권자로부터 별도의 허가를 받으면 이러한 조건들은 적용되지 않습니다.

저작권법에 따른 이용자의 권리는 위의 내용에 의하여 영향을 받지 않습니다.

이것은 [이용허락규약\(Legal Code\)](#)을 이해하기 쉽게 요약한 것입니다.

[Disclaimer](#)

Ph. D. DISSERTATION

Hybrid Mode Shaping with Auxiliary EM
Potential for Mitigation of B_1^+
Inhomogeneity in Ultra-High-Field
Magnetic Resonance Imaging

초고자장 자기공명영상의 B_1^+ 불균일성 완화를
위한 전자기 퍼텐셜 기반의
하이브리드 모드 성형 연구

BY

MINKYU PARK

FEBRUARY 2021

DEPARTMENT OF ELECTRICAL ENGINEERING AND
COMPUTER SCIENCE
COLLEGE OF ENGINEERING
SEOUL NATIONAL UNIVERSITY

Hybrid Mode Shaping with Auxiliary EM Potential for Mitigation of B_1^+ Inhomogeneity in Ultra-High-Field Magnetic Resonance Imaging

지도 교수 박 남 규

이 논문을 공학박사 학위논문으로 제출함
2021 년 2 월

서울대학교 대학원
전기·컴퓨터 공학부
박 민 규

박민규의 공학박사 학위논문을 인준함
2021 년 2 월

위 원 장 _____ 정 윤 찬 (인)

부위원장 _____ 박 남 규 (인)

위 원 _____ 이 중 호 (인)

위 원 _____ 오 정 석 (인)

위 원 _____ 신 중 화 (인)

Abstract

Hybrid Mode Shaping with Auxiliary EM Potential for Mitigation of B_1^+ Inhomogeneity in Ultra-High-Field Magnetic Resonance Imaging

MINKYU PARK

DEPARTMENT OF ELECTRICAL ENGINEERING AND

COMPUTER SCIENCE

COLLEGE OF ENGINEERING

SEOUL NATIONAL UNIVERSITY

Magnetic resonance imaging (MRI) is one of the most popular diagnostic imaging tools with its safety and applicability. By increasing the strength of operating B_0 , MRI has improved image quality, and recent research has enabled the imaging modality to increase the operating B_0 fields over 7T, which is in the ultra-high-field (UHF) range. UHF MRI has various advantages, including the enhancement of the signal-to-noise ratio (SNR), spectral and spatial resolutions, and contrast. Especially, UHF MRI has an irreplaceable strength in precise scanning of the brain tissue to examine

various neurological disorders. Nonetheless, the increase of the operating magnetic field causes the severe issue of RF B_1^+ field inhomogeneity, which is detrimental to homogeneous retrieval of the intensity, SNR, and contrast in MR image.

To tackle the critical issue of inhomogeneity, a multitude of approaches for shimming the B_1^+ inhomogeneity have been proposed. Among them, RF passive shimming by pad structure filled with dielectric materials has proven its validity as a safe and well-compatible solution applicable to clinical applications. While successful in controlling the field distribution, most of the past efforts utilizing the local enhancement of B_1^+ in the vicinity of the pad structures, especially those in contact with the body, often resulted in deterioration of the global B_1^+ homogeneity over the ROI. Therefore, a study on a scheme for achieving the global homogeneity of B_1^+ is required.

In this dissertation, we propose the notion of the mode shaping based on the evanescent coupling of the electromagnetic potentials to address the issue of B_1^+ field homogeneity. Treating the human head as a resonator, we apply an auxiliary potential well evanescent coupled to the head potential, to investigate the effects of the auxiliary potential configuration on the mode shaping and the resultant field homogenization. From the analysis and optimization, we obtain a robust mode shaping pad solution to achieve 2D global homogenization of axial B_1^+ field for the phantom of various geometry and the realistic voxel model of heterogeneous materials, which is applicable to the conventional 2D MRI scanning. Furthermore, extending the mode

shaping approach with symmetry breaking, we propose the mode shaping solutions for 3D global homogenization of B_1^+ field. For the practical assessment of the feasibility of the mode shaping solutions, the SAR and robustness analysis of the solutions are also conducted. We believe that this study will expand the capability of the RF passive shimming in UHF MRI by providing an unconventional viewpoint and systematic guideline for the mitigation of B_1^+ inhomogeneity.

Keywords : Ultra-high-field magnetic resonance imaging, RF B_1^+ inhomogeneity, RF passive shimming, Mode shaping, Auxiliary electromagnetic potential

Student Number : 2013-20790

Table of Contents

Abstract	i
Table of Contents.....	iv
List of Tables	viii
List of Figures	ix
Chapter 1. Introduction	1
1.1 Ultra-high-field magnetic resonance imaging:	
promising scheme for clinical imaging.....	2
1.2 Inhomogeneity problem in UHF MRI: Motivation	5
1.3 Dissertation overview	7
Chapter 2. Theory and method for the B_1^+ shimming	9
2.1 Electromagnetics in the UHF MRI	10

2.1.1 Principal physics of MRI system in view of electromagnetics	10
2.1.2 Issue of RF B_1^+ field inhomogeneity in UHF MRI.....	14
2.2 B_1 shimming in UHF MRI.....	17
2.2.1 Current approaches and achievements for B_1^+ shimming...	17
2.2.2 Background and motivation of our strategy for B_1 shimming: mode shaping pad	21
2.3 Optical mode shaping based on evanescent coupling for mitigation of B_1^+ inhomogeneity	23
2.3.1 UHF MRI systems as an optical waveguide	23
2.3.2 Mode shaping via evanescent coupling in optics.....	24
2.3.3 Evanescent coupling of electromagnetic potentials in UHF MRI.....	26
2.4 Conclusion	29

Chapter 3. Hybrid mode shaping with auxiliary EM potential for global 2D homogenization..... 30

3.1 Mode shaping for 2D MRI scanning.....	31
3.2 Concept of hybrid mode shaping with auxiliary EM potential	34
3.3 Optimization process.....	38
3.4 Effect of the phantom and pad geometry and other material parameters of the pad	47
3.5 Effect of the inhomogeneous distribution of materials:	

human voxel model	52
3.6 Effect of the mode shaping potential pad on the SAR distributions	56
3.7 Robustness and stability of the mode shaping solution.....	59
3.8 Conclusion.....	61
 Chapter 4. Hybrid mode shaping with auxiliary EM potential for global 3D homogenization.....	63
4.1 Mode shaping for 3D MRI scanning.....	64
4.2 Hat pad potential for lower-order mode excitation	66
4.3 Asymmetric shifted pad potential	72
4.4 Effect of the shifted potential pad on the SAR distribution	79
4.5 Robustness of the mode shaping with asymmetric potential pad.	81
4.6 Conclusion.....	83
 Chapter 5. Conclusion.....	84
 Appendix A. Supplements for Chapter 3	86
A.1 Material and geometry for the MIDA voxel model.....	86
A.2 Excitation with realistic TEM coils.....	91
 Appendix B. Supplements for Chapter 4	93
B.1 Cylinder can solution for the global homogenization	93
 Appendix C	97

Bibliography	98
Abstract in Korean.....	109

List of Tables

Table 3.5.1 Electromagnetic properties of main materials composing the human voxel model MIDA. Tissues of the brain are highlighted with yellow shade, which constitutes the ROI for assessing the B_1^+ homogenization.	53
Table A.1.1 Electromagnetic material parameters composing the MIDA voxel. Brain tissues are highlighted with yellow shade.....	89

List of Figures

Figure 1.1.1 MR images for the brain with the system operated at 1.5 T and 7 T. The top row illustrates the T2*-weighted image scanned at 7 T compared with the 3 T image. The bottom row depicts enhanced sensitivity and spatial resolution with the axial images obtained by MRI at 1.5 T and 7 T [54].....	4
Figure 2.1.1 Structural illustration of a magnetic resonance imaging scanner [68].	11
Figure 2.1.2 Principal physics of MRI system in view of electromagnetics. (a) A schematic of the excitation system with a main magnet generating static B_0 field and an RF coil producing B_1 pulse for the magnetic resonance imaging [69]. (b) Alignment of proton spins composing the magnetization under no external magnetic field (left) or static magnetic field B_0 (right) [70]. (c) Precession of a spin around B_0 magnetic field with Larmor frequency of $\omega_L = \gamma * B_0$ [70]. (d) Excitation of a spin by an RF pulse of B_1 at Larmor frequency of $\omega_L = \gamma * B_0$ to flip the longitudinal magnetization into the transverse plane [71]. (e) Reception of the signal induced by the magnetization in precession [70]. (f) Slice selection by the gradient field shifting the Larmor resonant frequency. z-slice selection, in this case [70]. (g) Gradient in 3-	

dimensional directions for spatial encoding [70].	12
Figure 2.1.3 Inhomogeneity problem in UHF MRI. The 7 T MR images in the coronal (left) and axial (right) plane are obtained by a birdcage coil designed for highly uniform distribution of B_1^+ field. Central brightening of the images due to the dielectric effect of the RF wave is shown [77].	16
Figure 2.2.1 Current approaches with B_1^+ passive shimming. B_1^+ field manipulation by (a) Dielectric pad filled with water [85], (b) Dielectric pads of high permittivity materials [88], (c) Metasurface [92], and (d) Hybridized meta-atom [93].	20
Figure 2.3.1 Mode shaping via evanescent coupling in optics. (a) Double clad fiber (DCF) [100]. (b) Mode shaping in multicore fibers [98]. (c) The nonlinear coherent coupler [96].	25
Figure 3.2.1 The concept of evanescent mode coupling for MRI B_1^+ shimming with the pad potential. (a) Schematic of the proposed MRI B_1^+ shimming system: RF coil (gray), phantom (yellow), and cylindrical pad (blue). (b) The corresponding permittivity potential layout along the radial direction: phantom (yellow), air-gap barrier (black), and pad (blue line). (c) The plot of the B_1^+ field amplitude along the radial direction at the center of the axial plane ($z = 0$): phantom-only (yellow curve), pad-potential-only (blue curve), and both the phantom and pad potentials (red curve). The yellow- and blue-shaded region each corresponds to the brain phantom and pad.	37
Figure 3.3.1 Effects of the pad permittivity ϵ_p (pad potential depth) on the mode shaping. Normalized field amplitude in the sagittal plane ($\theta = 0$). Contour lines represent the $B_1^+ / B_{1^+ \text{center}}$ values of 1 (red), 1/2 (yellow), and 1/4 (blue). The region of interest, i.e., the cylinder phantom, is marked with a black rectangle. The pad is marked by the black-dashed rectangles. The width of the air-gap	

potential barrier w_b is set at 2 cm. The width of the pad potential well w_p is set at = 2 cm.39

Figure 3.3.2 | Coupling of the potential well for various pad potential depth. (left column) Phantom potential well dominant system ($\epsilon_p = 40$). (center column) Pad potential well dominant system ($\epsilon_p = 180$). (right column) Much deeper pad potential system ($\epsilon_p = 280$). Higher-order mode coupling is failed. (upper row) The permittivity potential layout along the radial direction. The eigenvalue of the dominant mode is marked with the gray dashed line. (middle row) B_1^+ field amplitude along the radial direction at the center of the axial plane ($z = 0$). phantom-only (yellow curve), pad-potential-only (blue curve), coupled-system (red curve). (lower row) Normalized field amplitude in the sagittal plane for pad-potential-only cases.42

Figure 3.3.3 | Effects of the pad potential width w_p on the mode shaping. (a) Max/min ratio (left axis, solid curves) and node position (right axis, dotted curves) obtained for various w_p (1~3 cm), at the central plane of the ROI ($z = 0$). (b) Relation between w_p and ϵ_p , obtained for the minimum MmR = 1.2. (c-e) Mode profile in the sagittal plane ($\theta = 0$). Potential barrier width $w_b = 2$ cm.43

Figure 3.3.4 | Effects of the air-gap potential barrier width w_b on the mode. (a) Potential distribution in the radial direction. (b) Max/min ratio obtained for various w_b values at the central plane of the system ($z = 0$). (c-f) Mode profile in the sagittal plane ($\theta = 0$). $\epsilon_p = 180$, and $w_p = 2$ cm.45

Figure 3.3.5 | Effects of the pad potential depth on the mode shaping for contact pad case. Mode flattening effect in the contact potential case is not significant in comparison to that in the evanescently coupled potential case.46

Figure 3.4.1 | B_1^+ homogenization tested with a spheroidal phantom (long axis

= 9 cm, short axis = 7 cm). For the pad, $\epsilon_p = 188$, $w_b = 2$ cm, and $w_p = 2$ cm. (a) Mode profile in the sagittal view. (b) Max/min ratio at different axial slices (z -positions). (c) Axial images along the z -direction.....48

Figure 3.4.2 | B_1^+ homogenization tested with a spheroidal phantom using the gap-matched pad. For the curved pad, $\epsilon_p = 162$, $w_b = 2$ cm, and $w_p = 2$ cm. (a) B_1^+ field distribution in the sagittal plane. (b) Max/min ratio at different axial slices (z -positions). Much more homogenization is achieved by gap-matching.....50

Figure 3.4.3 | Effect of the magnetic permeability and the loss of the pad. (a-c) Mode profile for a magnetic pad of $\mu_p = 2, 4, 6$. (d-f) Effects of pad loss ($\sigma_p = 0.01, 0.2, 0.5$) on the mode shaping. $\epsilon_p = 180$. For all cases, $w_b = 2$ cm, and $w_p = 2$ cm.....51

Figure 3.5.1 | B_1^+ homogenization tested with a human head voxel model, MIDA. (a) Sagittal image without mode shaping pad potential. Central brightening is observed. (b) Modal profile with the mode shaping pad in the sagittal view. For the pad, $\epsilon_p = 131.5$, and $w_p = 2$ cm. w_b is not strictly defined, unlike for the phantom case, due to the asymmetric geometry of the voxel model. The inner radius of the cylindrical pad is set at 11.5 cm, and the height of the cylindrical pad is 24 cm. (c) Max-to-min ratio value as the figure of merit at different axial slices. It is noted that axial slice is defined in $z = 0$ cm to $z = 10$ cm. (d) Axial images corresponding to the z -cuts.....54

Figure 3.6.1 | Effect of the mode shaping potential pad on the SAR distributions. SAR distributions in the sagittal plane for the case of (a) MIDA voxel only and (b) MIDA voxel with the mode shaping pads. (c) SAR images at different axial cuts for each case. The SAR values are calculated for the ROI except for the node region ($z = -4$ cm \sim -3 cm and $z = 3$ cm \sim 4 cm), and for scanning

the node region, SAR values should be scaled by a factor of 8.6.
..... 58

Figure 3.7.1 | Robustness or stability of the mode shaping and the B_1^+ homogenization. (a) Robustness or stability of the mode shaping solution tested against the variations in the geometry (volume reduction by 10%) and position (forward, backward, and lateral bending by 10°) of the human head. (b) The average reduction of MmR corresponding to the four variations. The maximum and minimum levels are marked with a blue dashed line and a red dashed line, respectively.60

Figure 4.2.1 | Effects of the hat pad permittivity ϵ_h (pad potential depth) on the mode shaping. The hat pads are composed of two circular dielectric disks with 11 cm radius and 2 cm height, located on the top and bottom of the cylindrical phantom.....68

Figure 4.2.2 | Mode shaping with hat and necklace pad potential for the cylindrical and the spheroidal phantom. Symmetric hat potential on the top and bottom of the phantoms (top row) and asymmetric hat-necklace potential (bottom row) are applied. For asymmetric cases, the neck is composed of the same phantom material, and the region of it is marked with a solid gray box. The necklace pad surrounding the neck is marked with gray dashed lines..... 70

Figure 4.3.1 | Effects of the pad positional asymmetry on the mode shaping. No variance of the structure of the potential pad under positional shifting. The height of the pad is fixed at 24 cm, the width of the pad potential well w_p is set at 2 cm, and air gap width w_p is 1 cm. All the shifted potential pads have permittivity ϵ_p of 135. ROI covering the upper brain is marked with a white dotted line... 74

Figure 4.3.2 | Field pattern in axial slices in B_1^+ shimming by the shifted pad potential. (a) Field distribution under the shimming by the shifted potential in sagittal view. (b) MmR values over the axial slices. (c)

Axial images for each slice. Normalized with the maximum B_1^+ field inside the phantom for each case.....	76
Figure 4.3.3 Shifted asymmetric pad potential applied for B_1^+ field homogenization in the MIDA voxel case. (a) Sagittal image with a shifted asymmetric pad. (b) Max-to-min ratio value as the figure of merit at different axial slices. (c) Corresponding axial images.	78
Figure 4.4.1 SAR analysis for the human head voxel without and with the mode shaping pads. The sagittal SAR images corresponding to the turbo spin-echo sequence for the case of (a) MIDA voxel only and (b) MIDA voxel with the mode shaping pad. (c) Corresponding axial SAR images. SAR at the center of the cerebrum is depressed by the implication of the pad.	80
Figure 4.5.1 Robustness of the global B_1^+ homogenization. (a) Robustness of the capacity to globally homogenize B_1^+ field against three positional variations and the geometrical variation is tested. (b) Under the variations, both averaged MmR and GMmR of the human in neutral position are changed within 5%.	82
Figure A.1.1 Sagittal cut of MIDA voxel model for (a) whole head (b) brain.	90
Figure A.2.1 Comparison of the sagittal images obtained by the MRI system with realistic coils and ideal coils. (a) B_1^+ field distribution in the sagittal plane obtained from MRI system equipped with a realistic eight elements TEM coils. (b) Sagittal field profiles in the case of excitation by the MRI RF system with the ideal sources.	92
Figure B.1.1 Schematic of MRI B_1^+ inhomogeneity mitigating system (a) with cylindrical dielectric matching layer and (b) with a spheroidal layer. RF coil (gray), spheroidal phantom (yellow), and matching layer (blue) of thickness w_m and electric permittivity ϵ_m	94
Figure B.1.2 Effects of the matching layer permittivity ϵ_m and geometry on	

the GH. (a) B_1^+ Maximum-to-minimum ratio over the phantom with cylindrical layer, spheroidal layer, and the air-gapped-cylinder layer. (b) Sagittal ($\theta = 0$) normalized B_1^+ field profiles of the phantom with no matching layer ($\epsilon_m = 1$), and (c) with the cylindrical layer of $\epsilon_m = 60$ and $w_m = 4$ cm (point indicated by an arrow in Figure. B.1.2a). The phantom (solid black ellipse), and the matching layer (black-dashed rectangle). 94

Figure B.1.3 | Mode profiles in the sagittal view for various geometry of the layer: (a) $w_m = 4$ cm cylinder of the phantom material ($\epsilon = 74.2$, $\sigma = 0.87$ S/m), (b) $w_m = 4$ cm spheroid of $\epsilon_m = 60$, and (c) $w_m = 4$ cm cylinder of $\epsilon_m = 60$ with 1 cm air gap between the layer and the phantom. 95

Figure B.1.4 | Effects of the cylindrical layer dimension w_m on the GH over the ROI. (a) Max/min ratio of the phantom with the layer of $w_m = 2$ cm, 3 cm, 4 cm, and 5 cm. (b) Sagittal mode profile of the matched case with the layer of $w_m = 3$ cm, $\epsilon_m = 80$, (c) and with the layer of $w_m = 5$ cm, $\epsilon_m = 50$ 95

Figure B.1.5 | Mode profile for a matching layer of more realistic geometry. The central part of the $\epsilon_m = 60$ layer is equivalently replaced with the air-gapped thinner layer of higher index ($w_m = 2$ cm, $\epsilon_m = 100$), marked with dotted rectangles. 96

Chapter 1

Introduction

As the opening chapter, this chapter gives an overview of the recent progress and challenges of ultra-high-field magnetic resonance imaging. We introduce the advantages of the imaging modality as the main subject of this dissertation. For the motivation of the dissertation, the issue of B_1^+ field inhomogeneity involved in ultra-high-field MRI is discussed. In the last part of the chapter, the outline of the dissertation is presented.

1.1 Ultra-high-field magnetic resonance imaging: promising scheme for clinical imaging

Since the advent of the concept in the 1970s, magnetic resonance imaging (MRI) has proven its validity to be one of the most popular diagnostic imaging tools with its influential and unique figures [1-9]. Based on the nuclear magnetic resonance (NMR) phenomenon, MRI is a safe and non-invasive imaging technique without the use of ionizing radiation, which is mainly distinguished from the other techniques such as X-rays, computed tomography (CT), positron emission tomography (PET), and single-photon emission computed tomography (SPECT) imaging [10, 11]. This examination safety makes the imaging technique's applicable range broaden to patients vulnerable to the effects of radiation, such as pregnant women, children, and older adults. The capability to obtain the MR image for any part of the human body is also one of the main advantages of MRI. Especially for imaging soft tissue (e.g., bone marrow, ligaments, cartilage) and organs, including the brain or the heart, the performance of MRI is superior to any other imaging schemes [12-19]. Besides scanning anatomical structures of the human body, MRI provides dynamic physiological information such as blood circulation through blood vessels and organs, perfusion, and blood oxygen level-dependent (BOLD) MR signals, to form the backbone of the functional MRI

(fMRI) [20-26].

Despite the advantages of the modality, the additional improvement of the image sensitivity has been required for the various applications. Resolution of images mainly determining the quality of the MR images basically depends on the strength of the magnetic field B_0 of the MRI system [27, 28], and most currently used MRI is operating at 1.5 Tesla (T) or 3 T. With this motivation, recent research has enabled the increase of the operating B_0 fields over 7 T, which is in the ultra-high-field (UHF) range. UHF MRI has additional advantages besides improving the sensitivity of the image, which include enhancing the signal-to-noise ratio (SNR), spectral and spatial resolutions, and contrast (Figure 1.1.1) [29-43]. With these functional merits, UHF MRI has a strength, especially in precise scanning the brain tissue, to examine various neurological disorders, including degenerative brain disease, brain tumors, cerebrovascular disease, and epilepsy, being unable with lower B_0 MRI systems [44-52]. 7 T MRI for human imaging has been used for the research fields since the early 2000s and has extended their use for clinical applications in 2017 after approval by the FDA [53].

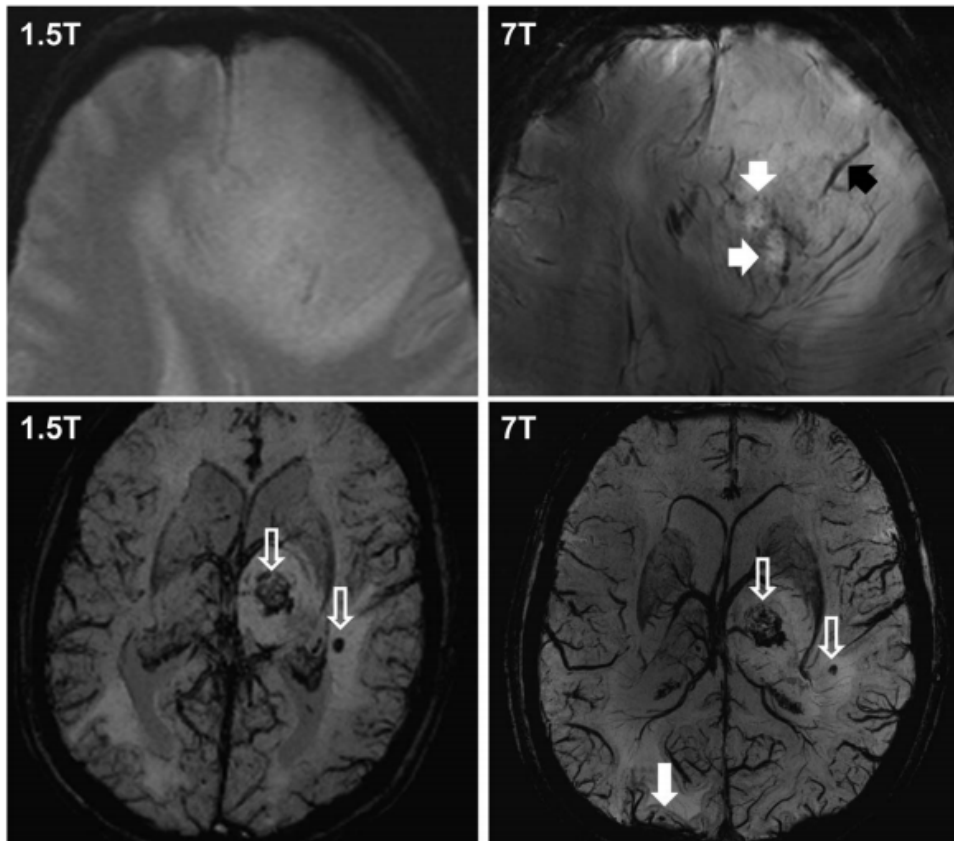


Figure 1.1.1 | MR images for the brain with the system operated at 1.5 T and 7 T. The top row illustrates the T2*-weighted image scanned at 7 T compared with the 3 T image. The bottom row depicts enhanced sensitivity and spatial resolution with the axial images obtained by MRI at 1.5 T and 7 T [54].

1.2 Inhomogeneity problem in UHF MRI:

Motivation

Nonetheless, the increase of the operating magnetic field causes some undesirable side effects to the proper operation of UHF MRI. To make the best use of various advantages of strengthening the magnetic field described in the previous sub-chapter (chapter 1.1), these detrimental effects need to be overcome. These challenges include clinical, practical, and technical issues such as patient comfort, safety, and cost [55-58]. Among the issues, field inhomogeneity problems overwhelm the other difficulties as the physical limitations, which causes the other problems subsequently and limits the benefits of increasing the magnetic field. Inhomogeneity of the static magnetic field B_0 is caused by a difference in magnetic susceptibility at the tissue-air boundary and tissue-bone boundary [59], exacerbated by scaling the strength of applied B_0 . This disturbance of the field can lead to producing image artifacts such as signal loss and geometric distortions [60, 61]. The most challenging problem to be overcome in UHF MRI is to address the management of the inhomogeneity of RF transmit field B_1 [47], which is a more severe issue because the imaging scheme is sensitive to the change of RF pulses excited by the standard conventional MRI system. With the increase of the main magnetic field B_0 , the corresponding RF operating wavelength also decreases and becomes comparable to the size of the human

body, resulting in a considerable phase effect of the field [62]. By this material-dependent effect, B_1 fields are spatially non-uniformly distributed with the pattern of increase in the central region and reduction in the periphery over the human body, which is detrimental to homogenous retrieval of the intensity, SNR, and contrast in MR image [63-66].

1.3 Dissertation overview

This dissertation consists of five chapters.

Chapter 1 briefly introduces the necessities and challenges of ultra-high-field magnetic resonance imaging, including the issue of B_1^+ field inhomogeneity motivating this study.

Chapter 2, with the electromagnetics involved in the issue about B_1^+ field in UHF MRI, provides the introduction of existing strategies for tackling the B_1^+ inhomogeneity problem in UHF MRI and limitations of those solutions, presenting the concept of optical mode shaping as the theoretical background of our alternative strategy for B_1^+ shimming.

In chapter 3, the notion of mode shaping via evanescent coupling of electromagnetic potentials for mitigating inhomogeneity of RF B_1^+ fields is investigated analytically and numerically with the scheme for the global 2D homogenization of axial B_1^+ suggested. In addition, design methods for the auxiliary mode-shaping potentials with additional degrees of freedom are also provided. A numerical experiment demonstrating the validity of the mode shaping solution for the realistic human voxel model is presented.

Chapter 4 shows the possibility of applying the concept to the 3D volume scanning, targeting a range of brain of ROI. By extending the concept of the mode shaping through potential coupling to the symmetry breaking cases, the global homogenization of the B_1^+ field is demonstrated.

Chapter 5 summarizes the hybrid mode shaping based on the coupling of the electromagnetic potentials for the homogenization of the RF B_1^+ in UHF MRI, which is the coverage of this dissertation.

Chapter 2

Theory and method for the B_1^+ shimming

To deal with the issue of B_1^+ inhomogeneity in UHF MRI, we employ a concept of optical mode shaping with evanescently coupled auxiliary electromagnetic potential, which is based on a rather unconventional approach. To show the notion systematically, we start this chapter with a brief review of electromagnetics related to B_1^+ field inhomogeneity and common approaches for B_1^+ shimming, and then we introduce the notion of hybrid mode shaping comparing with the conventional methods.

2.1 Electromagnetics in the UHF MRI

2.1.1 Principal physics of MRI system in view of electromagnetics

MRI is the medical imaging technique based on the nuclear magnetic resonance (NMR) phenomenon, which is the atomic reaction of the magnetization to external magnetic fields. Precisely, a spin of proton consists of the magnetization, and the net magnetization vector composed of a group of spins is zero (by thermal energy) under no external magnetic fields. When an external static magnetic field called B_0 is applied, this magnetization becomes aligned in a direction parallel to the B_0 field (z -direction conventionally) by the precession of the net magnetization around the B_0 field with Larmor frequency of $\omega_L = \gamma * B_0$ (Figure 2.1.1, Figure 2.1.2 a-c). In this situation, applying an RF pulse of B_1 at the Larmor resonant frequency flips the longitudinal magnetization into the transverse plane, where the flip angle is proportional to the magnitude and duration of the B_1 field, described by $\theta_{flip} \sim 2\pi\gamma * B_1 * T_{pulse}$ (Figure 2.1.2 d). In the period of B_1^+ pulse turned off, RF coils placed orthogonal to the longitudinal plane pick this precession at the Larmor frequency by Faraday's law of induction, and this signal composes the source to be imaged (Figure 2.1.2 e).

Furthermore, to form an image based on the background phenomenon of the magnetic resonance, MRI uses spatial gradient fields added to the background field B_0 , shifting the operating resonant frequency slightly different from the Larmor frequency (Figure 2.1.2 f). This notion of spatial encoding enables the imaging scheme to select the slice plane to be scanned with the gradient in z (longitudinal)-axis usually, and to specify the spatial information of the selected slice in the xy -plane (transverse plane) by the frequency and phase encoding (Figure 2.1.1, Figure 2.1.2 g). This spatially encoded magnetization detected by receiving coils becomes a signal for the construction of the MR images after post-processing based on the Fourier transform (FT) to image reconfiguration [67].

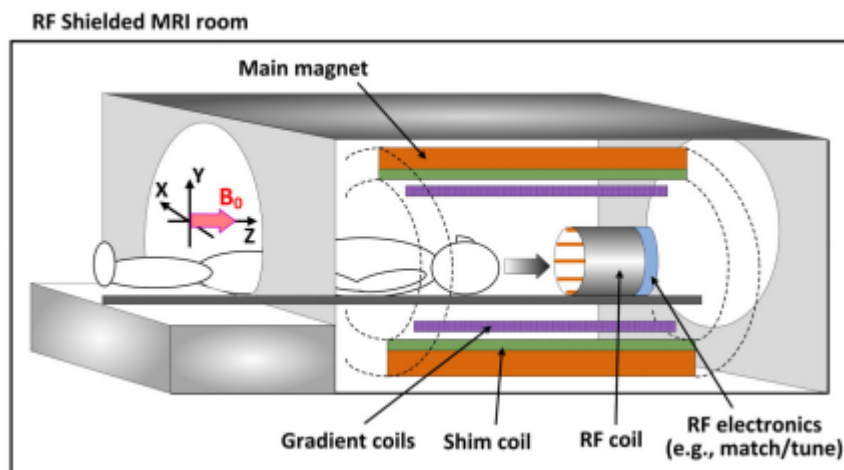


Figure 2.1.1 | Structural illustration of a magnetic resonance imaging scanner [68].

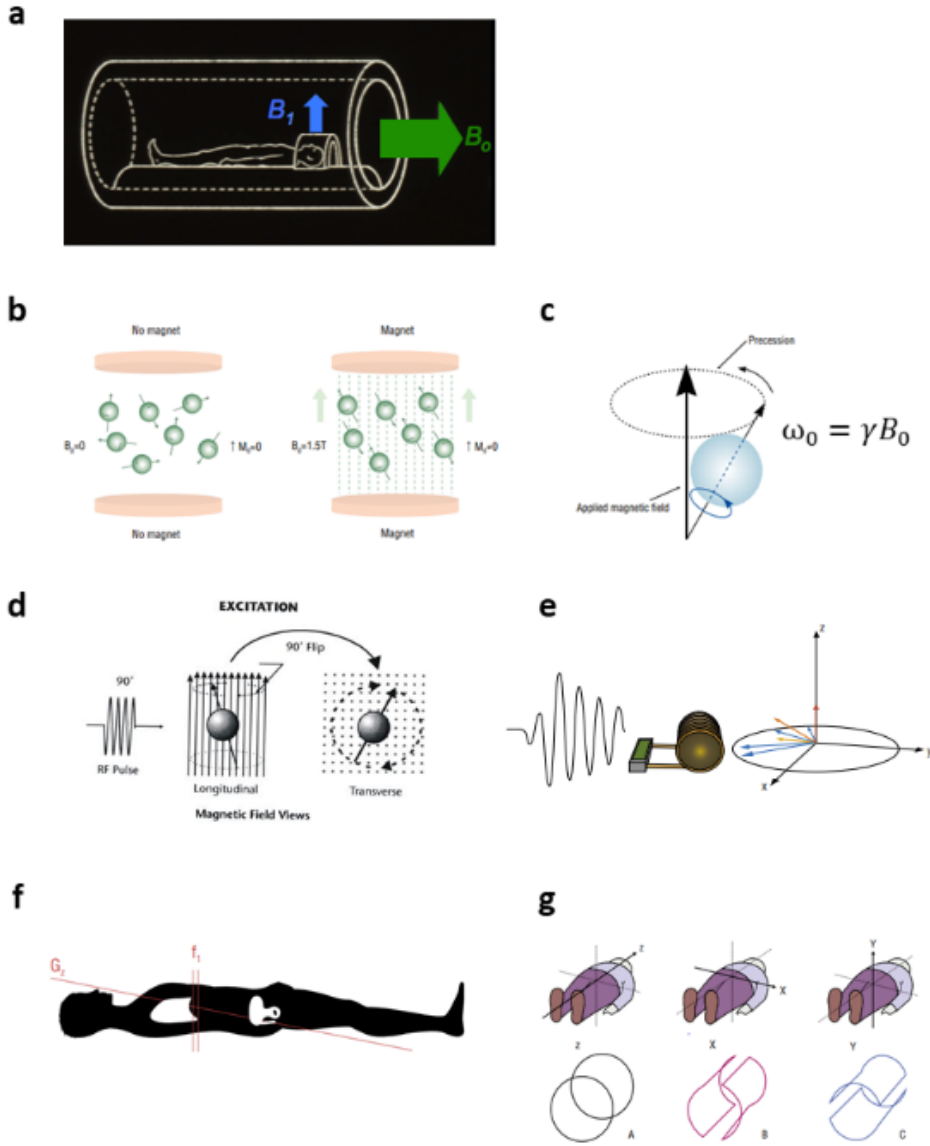


Figure 2.1.2 | Principal physics of MRI system in view of electromagnetics.

(a) A schematic of the excitation system with a main magnet generating static B_0 field and an RF coil producing B_1 pulse for the magnetic resonance imaging [69]. (b) Alignment of proton spins composing the magnetization under no external magnetic field (left) or static magnetic field B_0 (right) [70]. (c) Precession of a spin around B_0 magnetic field with Larmor frequency of

$\omega_L = \gamma * B_0$ [70]. **(d)** Excitation of a spin by an RF pulse of B_1 at Larmor frequency of $\omega_L = \gamma * B_0$ to flip the longitudinal magnetization into the transverse plane [71]. **(e)** Reception of the signal induced by the magnetization in precession [70]. **(f)** Slice selection by the gradient field shifting the Larmor resonant frequency. z -slice selection, in this case [70]. **(g)** Gradient in 3-dimensional directions for spatial encoding [70].

2.1.2 Issue of RF B_1^+ field inhomogeneity in UHF MRI

In principle, achieving the image with the MRI system is based on the implication of uniformly distributed external magnetic field B_1^+ over the scanning region, which is directly related to the resultant intensity profile of the image. This assumption is approximately valid for the conventional MRI system for brain scanning, which is operated at $B_0 = 1.5$ T or 3 T, where the corresponding Larmor wavelength is far longer compared to the size of the sample. As the operating B_0 goes higher, the corresponding Larmor wavelength is shorter and shorter with the rise of the Larmor resonant frequency and then becomes comparable or shorter than the size of the tissue. Quantitatively, the wavelength λ of an electromagnetic wave propagating in tissue is inversely proportional to the refractive index n of the dielectric medium or square root of the relative permittivity ϵ_r of the medium, which can be expressed as

$$\lambda = \frac{2\pi c}{\omega} \cdot \frac{1}{\sqrt{\epsilon_r}} \quad (2.1)$$

where c refers to the propagation speed of the wave in free space and ω is angular frequency [72]. For the grey matter of the brain, the relative permittivity is equal to approximately 60 at $B_0 = 7$ T, and then the Larmor wavelength λ_L of 12 cm inside the human body is shorter than the dimension of the body. In this case, the phase of the RF wave becomes no longer negligible, and wave behavior should be considered. Moreover, by the

presence of dielectric loss with electrical conductivity of tissue, wave penetrating the tissue becomes attenuated and loses their intensity for propagating through the medium. By the dielectric effects of high index and conductivity, the wavelength-shortened decaying RF wave forms the complicated and hard-to-predictable interference field pattern inside the human head with the complex distribution of tissue perturbing the field profile. Nevertheless, this human head generally presents the typical field pattern of a few-mode resonator constituted with high permittivity and conductivity materials surrounded by an air of much lower permittivity $\varepsilon = 1$ (e.g., bright in the central region, dark in the periphery) [73, 74], which is called ‘central brightening’ depicted in Figure 2.1.3.

Various causes engaged in the inhomogeneity of RF B_1^+ field, including the imperfect configuration of excitation, the interaction between the coils and sample to be scanned, or positional alignment of sample related to the excitation, have been reduced by calibration to a considerable extent. Even if these technical issues were entirely conquered, the fundamental and physical limitation of the dielectric effect is still alive and hinders the imaging scheme from obtaining uniform MR images. Moreover, this hard to handle issue becomes more deteriorated in scanning larger anatomical structure of the sample such as part of the human body or in operating the MRI system at higher B_0 field [75, 76].

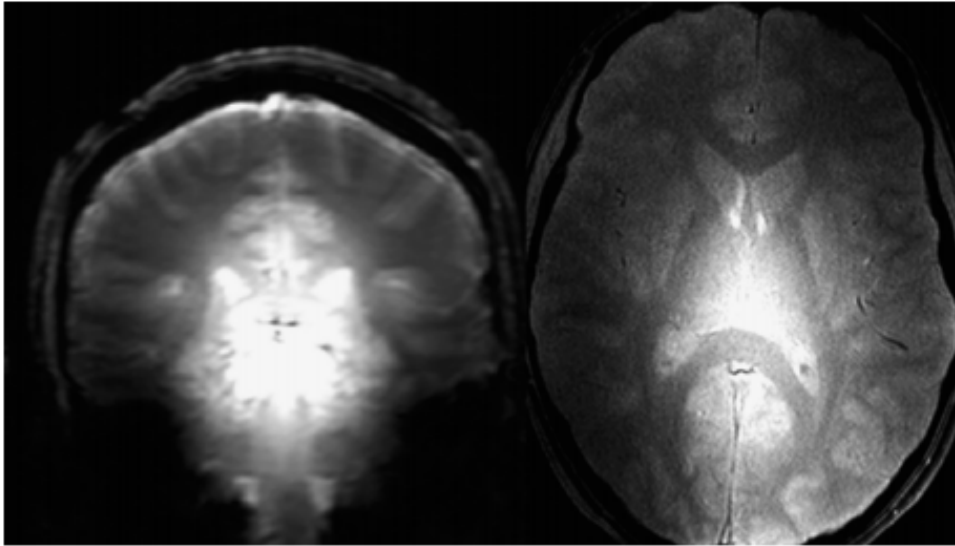


Figure 2.1.3 | Inhomogeneity problem in UHF MRI. The 7 T MR images in the coronal (left) and axial (right) plane are obtained by a birdcage coil designed for highly uniform distribution of B_1^+ field. Central brightening of the images due to the dielectric effect of the RF wave is shown [77].

2.2 B_1 shimming in UHF MRI

2.2.1 Current approaches and achievements for B_1^+ shimming

To tackle the critical issue of inhomogeneity and take advantage of the increased operating field in the UHF MRI system, a multitude of approaches for shimming the B_1^+ inhomogeneity have been proposed.

Employing novel designs of RF coils for excitation allows the hardware of the system equipped with the coils to overcome the inevitable restriction of the MRI system with the conventional RF coils. As the operating frequency of the system goes higher, distribution of B_1^+ excited by birdcage coil that is the most popularly accepted RF coil in the MRI systems at operating magnetic field under 3 T unavoidably experiences non-uniformity by its structure [78]. With escaping from the whole-connected structure, new design concepts have become the standard in UHF MRI, while the birdcage coil is also still regarded as the standard configuration of the coil. Especially, transverse electromagnetic (TEM) coil has successfully replaced the conventional birdcage coil, and this alternative design concept has been the basis for the following methods to deal with the issue of the B_1^+ inhomogeneity [79].

Developing effective forms of RF pulse to flip the net magnetization also has shown its validity in the RF field homogenization, and this concept of molding the shape of the excitation B_1^+ field has been successfully implemented in the conventional MR imaging system. Applying an adiabatic RF pulse design or a composite pulse shape are the representative examples [80, 81].

Parallel transmission (pTx) is also a promising notion of mitigating the B_1 inhomogeneity as the active RF shimming, which is based on the independent control of the multichannel coils. This concept has been expanded to molding the shape of the excitation signal from each coil, which includes the amplitude and the phase modulation [82, 83]. This gives the degrees of freedom for manipulating B_1 fields as the most flexible technique to modulate the RF signal excitation, resulted in improvement of homogeneity. Though having shown the possibility of higher degree B_1 control, this technique needs to overcome the regulation issue related to the specific absorption rate (SAR) and the workflow issues associated with computing power. For these reasons, only a few systems partially based on this notion have been approved for use in the field of clinical MRI [84].

Alternative common approaches for mitigating or shimming this B_1^+ inhomogeneity are to use the capacity to alter the B_1^+ distribution with high-permittivity materials (HPM), which is called RF passive shimming. Dielectric pads filled with water ($\epsilon \sim 78$ at 300 MHz) placed in contact with the head have been used to improve the sensitivity of the signal in the

peripheral region of the ROI (region of interest), especially in proximity to the high permittivity pads (Figure 2.2.1 a) [85]. Pads of mixtures of metal titanate and water have been employed to increase the permittivity of the pads so that they can be used in similar strategies (Figure 2.2.1 b) [86-91]. Structures with metallic inclusions, such as metasurfaces (Figure 2.2.1 c) and hybridized meta-atoms (HMAs) (Figure 2.2.1 d), have also been reported to manipulate field profiles at subwavelength scales [92, 93]. However, while successful in controlling the field distribution, most of the past efforts utilizing the local enhancement of B_1^+ in the *vicinity* of the pad structures, especially those in contact with the body, often resulted in deterioration of the *global* B_1^+ homogeneity over the ROI.

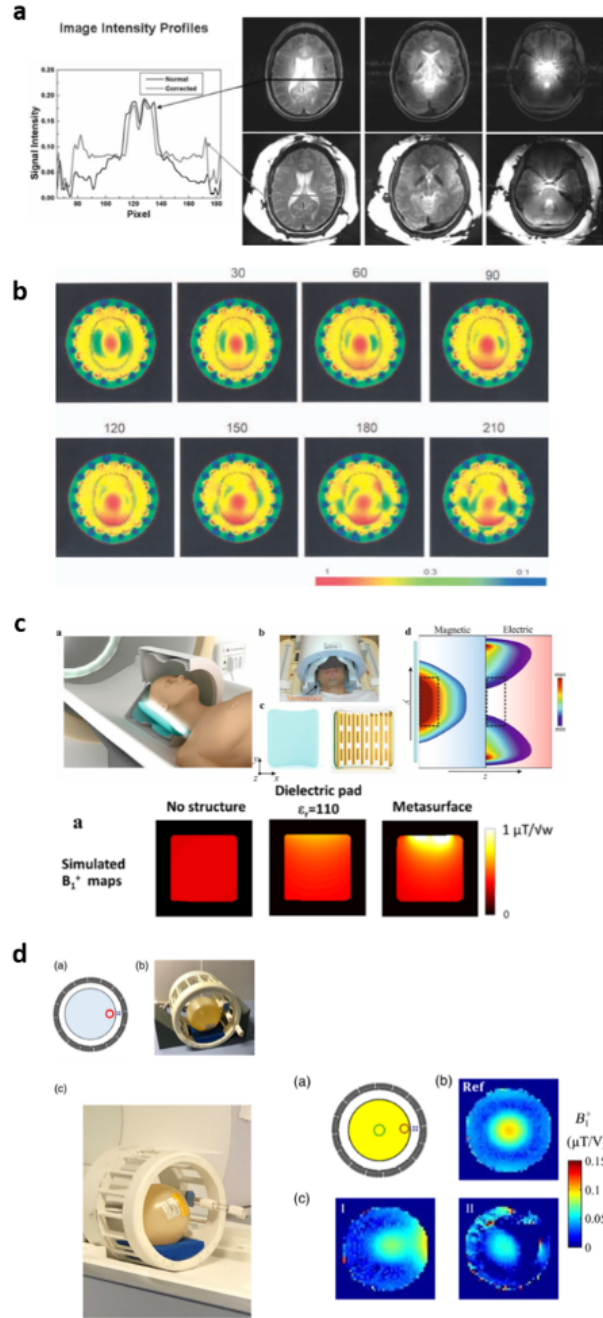


Figure 2.2.1 | Current approaches with B_1^+ passive shimming. B_1^+ field manipulation by (a) Dielectric pad filled with water [85], (b) Dielectric pads of high permittivity materials [88], (c) Metasurface [92], and (d) Hybridized meta-atom [93].

2.2.2 Background and motivation of our strategy for

B_1 shimming: mode shaping pad

Though having shown the possibility of a higher degree for B_1^+ control and improvement of B_1^+ homogeneity, currently proposed approaches have their own limitations that need to be overcome. Although they may be approved someday with proper confirmation or guarantee, the active RF shimming methods, including a new coil or pulse shape design, are not free from the safety issue now. Because clinical regulation for the patient is basically strict and conservative, the modification of the conventional MRI system is somewhat limited or prohibited for specific cases. Thus, we focus on the strategy for B_1^+ shimming based on the safety-verified concept of passive shimming with the pad structure.

The passive shimming by padding was a relatively conventional method with constraints of material and geometrical selection, causing the limitation of the field control capacity. With the chance to the introduction of dielectric pads of high index material or metamaterials, the passive shimming recently regain attention for improved higher-order manipulation of field distribution. Nevertheless, applications of the pad structure are mainly focused on the compensation of magnetic fields with the displacement current generated by the additional loading material in the vicinity of the target of the shimming, which is the original purpose of padding. This shimming strategy

involves an inevitable degradation of the fields in the other part of the region of interest, prohibiting the homogenization of the B_1 field for overall ROI in a fundamental manner. Though a few methods regarding the design of pad structure based on the optimizing algorithm to tackle the issue have been reported [94, 95], spatial coverage for the uniform distribution of the field with the single scanning is still restricted in the partial ROI. For the global field homogeneity, analysis of the mode ultimately determining the field distribution in an electromagnetic structure, the human head, is required, but the modal approach is still insufficient and infertile for now.

With this motivation, our strategy for mitigating B_1^+ inhomogeneity is based on the concept of mode, including examining how the modes are related to the field uniformity and are controlled to obtain a homogeneous distribution of B_1^+ field. For this, we utilize the achievements widely accepted in the current MRI system, such as the individually controllable TEM coils for improved uniformity of field in excitation and high index dielectric pads for mode control with a well-proven safety. While our scheme of modal shaping with an auxiliary electromagnetic potential described in the next section does not strictly depend on a specific material, the potential can be implemented using the pad structure, which we call mode shaping pad.

2.3 Optical mode shaping based on evanescent coupling for mitigation of B_1^+ inhomogeneity

2.3.1 UHF MRI systems as an optical waveguide

To clarify the situation, only crucial components of the MRI system regarding the interaction between the human body and the B_1^+ field are considered. This simplified MRI system modeling B_1^+ excitation is composed of three RF structures: the human body/head, RF B_1 coils in the cylindrical configuration, and the cylindrical shield. The tissues of high permittivity material make up the human body. This high permittivity body surrounded by an air of much lower permittivity ($\varepsilon = 1$) constitutes an electromagnetic resonator operating at the Larmor RF frequency under the excitation of the MRI RF field B_1^+ . The MRI system is seemingly different but similar to the situation commonly addressed in optics with different operating frequencies. Thus, we treat the system in terms of a cavity resonator or a waveguide with finite length under lateral excitation. The former focuses on the resonant with 3D structure, and the latter implies the symmetric propagation of the wave inside the body, and then both perspectives give us insights to analyze and tackle the issues associated with the MRI system.

2.3.2 Mode shaping via evanescent coupling in optics

Modal shaping with evanescent coupling has been employed as a proven technique in various applications of optics (Figure 2.3.1). This technique enables the manipulation of optical properties for the purpose of devices, such as power transfer, spin conversion, and phase matching [96-99]. Especially, double-clad W-type fibers use a higher-index outer cladding layer in combination with a lower-index inner cladding layer to tailor the modal confinement and dispersion properties, which is not achievable from simple core-clad structures (Figure 2.3.1 a) [100-102].

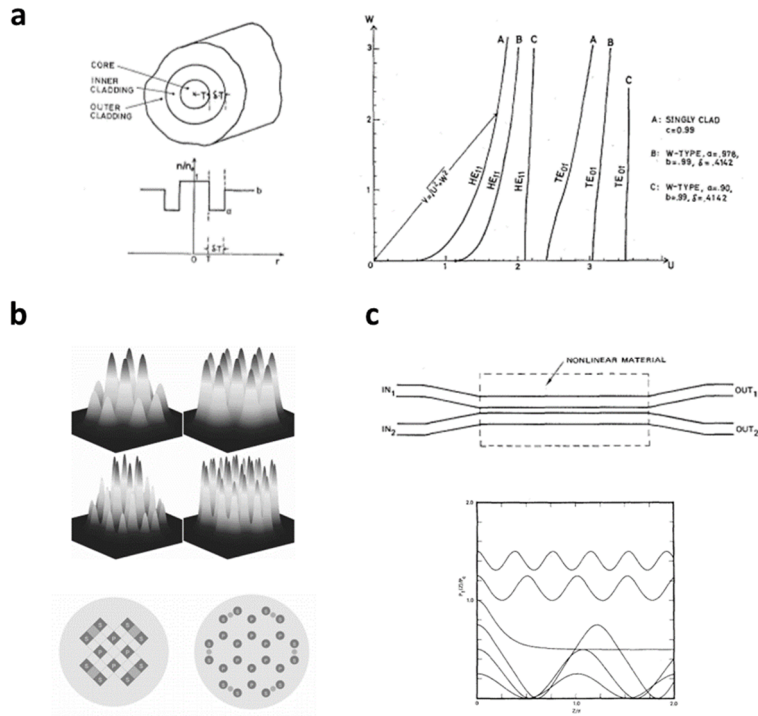


Figure 2.3.1 | Mode shaping via evanescent coupling in optics. (a) Double clad fiber (DCF) [100]. **(b)** Mode shaping in multicore fibers [98]. **(c)** The nonlinear coherent coupler [96].

2.3.3 Evanescent coupling of electromagnetic potentials in UHF MRI

For the purpose of molding the electromagnetic fields inside the human body for the MRI system, we employ the concept of doubly cladding fiber by applying an air-gapped (inner cladding) dielectric clad (outer cladding) which is a dielectric pad in terms of MRI B_1^+ shimming. Unlike the conventional configurations of double cladding optical fiber, the dielectric outer cladding layer has relative permittivity higher than that of the human head or body to magnify the effect of the layer. There are two main reasons why we use a high index material to compose the outer cladding layer. With a multilayered waveguide structure, the rule of refractive index says the wave tends to propagate in the high index region in which the propagation constant is highest (wave velocity is slowest) [103]. In these high index double cladding configurations, propagation of the wave excited by the RF MRI coils has to be dominated by the high-index outer cladding layer to determine the whole character of the double-clad waveguide. In this regard, the situation can be approximately translated into the consideration of the hollow cylindrical waveguide only system with the subsequent interaction between the core and the clad. In other words, the system works as the coils excite the hollow cylindrical waveguide of outer cladding only, and this waveguide interacts with the coupled core waveguide. Dominion is also essential so that the high

index layer focuses on the interaction between the core and cladding rather than on the effect of the external field on the core to retain the robustness of the solution, which is the second reason to use a high-index material for outer cladding.

From a different perspective, the description of the system in terms of the electromagnetic potential can be considered, with the analogy between the electromagnetic field describing the electromagnetic wave inside a dielectric waveguide and the wave function expressing the matter-wave inside the potential well. This electromagnetic and quantum mechanical analogy comes from the identical form of the governing equations, the Helmholtz equation and the Schrodinger equation, and the natures of an electromagnetic wave propagating associated with multilayered waveguides have been accounted for with the aid of the corresponding quantum mechanical model [104]. We utilize the model extended to the cylindrical waveguides in the cylindrical coordinate system for describing the double cladding waveguide MRI system with the potential-well model. The Schrodinger equation describing an electron in a 2D circular finite potential well is,

$$\frac{\partial^2 \psi(r)}{\partial r^2} + \frac{1}{r} \frac{\partial \psi(r)}{\partial r} + \frac{2m}{\hbar^2} (E - V(r)) \psi(r) = 0 \quad (2.2)$$

for $l = 0$ or $\frac{\partial}{\partial \theta} = 0$ case.

Helmholtz wave equation for a wave propagating along z -direction in a cylindrical waveguide is,

$$\frac{d^2 u(r)}{dr^2} + \frac{1}{r} \frac{du(r)}{dr} + (n^2(r)k_0^2 - k_z^2)u(r) = 0 \quad (2.3)$$

for $l = 0$ or $\frac{\partial}{\partial \theta} = 0$ from excitation symmetry.

With symmetry condition, these two equations are mathematically identical with these associations,

$$E \rightarrow -\frac{\hbar^2}{2m} k_z^2 \quad (2.4)$$

and

$$V \rightarrow -\frac{\hbar^2}{2m} n^2 k_0^2 \quad (2.5)$$

The quantum mechanical modeling allows the dielectric waveguide system to be interpreted in the potential-wells and accounts for the need to apply the additional potential well to the core-only system. The interpretation says the modes of the waveguide in terms of the bounded states of an electron in the potential well, allowing the well-known phenomena and properties used in the quantum mechanical worlds to be employed and analyzed in a much more straightforward manner in the electromagnetic counterpart we will solve. The tunneling effect of an electron wave function in the coupled potentials, especially, is considered for showing the effect of modal shaping inside the human body (the core of the cylindrical waveguide) via evanescent coupling of the *electromagnetic* potential wells.

2.4 Conclusion

In this chapter, fundamental physics in the MRI system related to producing an MR image in terms of electromagnetics is presented. Especially, we focus on the homogeneity issue of transmit RF B_1^+ field in UHF MRI, which takes a crucial role in the proper operation of the MRI system. With this motivation, we emphasize the necessity of the modal approach to tackle the inevitable problem of field inhomogeneity. Further, we propose the scheme of optical mode shaping via coupling of electromagnetic potentials to mitigate the B_1^+ field inhomogeneity and expand the capability of the passive RF shimming method.

Chapter 3

Hybrid mode shaping with auxiliary EM potential for global 2D homogenization

In this chapter, we apply the notion of optical mode shaping to UHF MRI systems to achieve global 2D homogenization of the axial B_1^+ field. We treat the MRI system, composed of the body and an RF B_1^+ coil, as a waveguide operating at the Larmor wavelength and then employ a high permittivity cladding layer (auxiliary electromagnetic potential well) to tailor the mode shape inside the body through controlling evanescent mode coupling. For this, we control three critical parameters of the RF B_1^+ waveguide: the depth of the pad potential, the width of the pad potential, and the width of the potential barrier between the body potential and the pad potential. With the concept of mode shaping, global homogenization of the axial B_1^+ field for both the phantom and the human voxel model is demonstrated.

3.1 Mode shaping for 2D MRI scanning

Most popular medical MRI scanning is based on the 2D slice cut scanning, which motivates us to handle the mode shaping suitable for B_1^+ homogenization in the 2D axial scanning for both its own purpose and the starting point for the extension of the mode-shaping scheme. To get this type of field pattern, we focus on forming the modal shape of the human-pad coupled system with radial propagation constant of the dominant mode lower in comparison to that of the fundamental human mode in the human-only system. Field distribution inside the cylindrical human resonator is characterized by the axial propagation constant k_z and the radial propagation constant k_ρ with the relationship between the constants given by

$$k_\rho^2 = k^2 - k_z^2, \quad (3.1)$$

and the propagation constant k in the resonator is given by

$$k^2 = \omega^2 \mu \epsilon_0 \epsilon_r - j\omega \mu \sigma, \quad (3.2)$$

related to the dielectric properties of the human body and the operating frequency of the MRI system [105]. According to the above relation, with the increase in k_z , the radial propagation constant k_ρ decreases, and the corresponding radial wavelength $\lambda_\rho = 2\pi/k_\rho$ increases, leading to the improvement of the field homogeneity in the radial plane.

To realize the increase in k_z of the system, two methods based on

loading dielectric materials in cylindrical configuration to fill the coil-to-shield space [106] or to fill the coil-to-human body space partially [107] have been proposed. Dielectric materials loaded in the coil-to-shield space heavily influence the propagation characteristic of the coil through changes in the current density which is a function of k_z in the axial direction [106]. While a promising candidate for reduction of radial variations of the RF field in conventional RF volume coils (e.g., shielded high-pass birdcage coils), the solution is difficult to be applied to some other types of coils which are working based on the invariance of the current distribution of the coils along the z -direction, including the low-pass birdcage coils, and the transverse electromagnetic (TEM) coils. Furthermore, loading materials in that region is prohibited by structural restriction of the coil geometry for some kinds of coils such as TEM coils (no room for the loading of the materials), and even if it is possible, this in-built solid structure strongly dependent on the geometry of the coils restricts the flexibility and the performance of the solution.

For the other proposed method, the author presents a dielectric load of cylindrical geometry placed in the coil as an example to alter the distribution of the transmit RF field [107]. Although the example implies the dielectric structure in the cylindrical configuration changes k_z in the MRI resonator as a function of the relative permittivity of the structure, the author suggests the cylindrical structure of high permittivity materials which supports higher k_z should not be used and be split into smaller discrete pad elements.

In this dissertation, based on the basic strategy to improve the radial RF field homogeneity by manipulating k_ρ and the corresponding λ_ρ , we propose the solution to achieve a transversely homogenous distribution of B_1^+ field over the whole region of the human body, compatible with various types of coils, including the TEM coils as well as the conventional birdcage coils. This is accomplished by applying dielectric materials in cylindrical geometry in the coils-to-human body region and by adjusting the geometrical and material parameters of the dielectric cylinder. In this setting, additional factors determining the field profile in the human body via adjusting the strength of coupling and the corresponding boundary conditions are incorporated, which is not considered in the previous works.

3.2 Concept of hybrid mode shaping with auxiliary EM potential

Considering the structure of MRI and the corresponding symmetries of the RF B_1^+ and DC B_0 fields, it is reasonable to approach the present solution as an electromagnetic boundary problem having dominant translational symmetry in the sagittal direction, with finite length. Since the uniformities of the B_1^+ field distribution in the radial and sagittal directions have a trade-off relation in a cylindrical phantom at a given Larmor frequency [107], we focus here on axial 2D MRI scanning, which is widely used in clinical applications. To start, we first simplify the MRI system to maintain the z -translational symmetry by assuming a *cylindrical* phantom and a *cylindrical* pad to minimize the mode mixing between the radial (r), sagittal (z), and azimuthal (θ) directions (Figure 3.2.1 a). In this setting, at a fixed sagittal (z -axis) height of the B_1^+ RF coil, phantom, and pad, the shaping of the mode is then determined by three control parameters: the depth of the auxiliary pad potential d_p , the width of the pad potential w_p , and the width of the potential barrier (air gap) w_b (Figure 3.2.1 b). We further note that in view of evanescent coupling, it is clear that the control of d_p and w_p will govern the amplitude and width of the B_1^+ field in the pad, while the control of the potential barrier w_b will determine the evanescent coupling and mode hybridization between the phantom and pad modes, achieving the resultant mode shaping in the

target ROI.

To assess the effect of mode hybridization from the proposed evanescent mode coupling, full-wave electromagnetic numerical analyses are carried out by using a FEM-based simulation tool (COMSOL Multiphysics). As the source of B_1^+ field RF excitation, we assume an idealized coil consisting of 16 surface current sources (rectangular, 1 cm x 18 cm) equally spaced on a cylinder (radius 15 cm, height 18 cm), where the impedance is appropriately matched. The currents on each source are sinusoidally driven with the same magnitude at a Larmor frequency of 300 MHz (corresponding to $B_0 = 7$ T) and are sequentially phase-shifted by $360^\circ/16 = 22.5^\circ$. It is noted that this sequential phase shift provides a homogeneous distribution of circularly polarized fields (i.e., B_1^+) with a coefficient of variation of less than 6% in the phantom loading region. The coil is surrounded by a cylindrical surface of the perfect electric conductor (PEC) with a radius of 17 cm and a height of 18 cm, modeling the shield of the coil for the MRI systems. To start, we also focus on the imaging of the head and employ a simplified head phantom, assuming a lossy dielectric cylinder (height of 18 cm, radius of 7 cm, relative permittivity of 74.2, conductivity of 0.87 S/m) made of an agar-agar gel [93]. For the dielectric pad encircling the phantom, we also assume a high-permittivity material and cylindrical geometry, to emphasize, not in contact but evanescently coupled to the head phantom through the potential barrier of the air gap. This shielded coil, cylindrical pad, and phantom constitute a coaxial structure, as shown in Figure 3.2.1 a,b, with air gaps in

between.

Figure 3.2.1 c shows the excited modes without or with the presence of pad potential: the yellow and the blue curve correspond to the B_1^+ field amplitude with the phantom only and the pad only, respectively, while the red curve shows that of the two potentials together, forming a hybridized mode exhibiting a flattened mode profile in the ROI of the head (at $z = 0$). Depending on the relative strength of the phantom and pad potentials with gaps in between, each potential dominates the overall mode profile in the MRI system, perturbed by the other potential. It is also critical to note that for a pad potential of sufficiently high permittivity, higher than that of the phantom, the behavior of the coupled mode is dominated by the pad potential and not greatly perturbed by the geometry or permittivity distribution of the phantom.

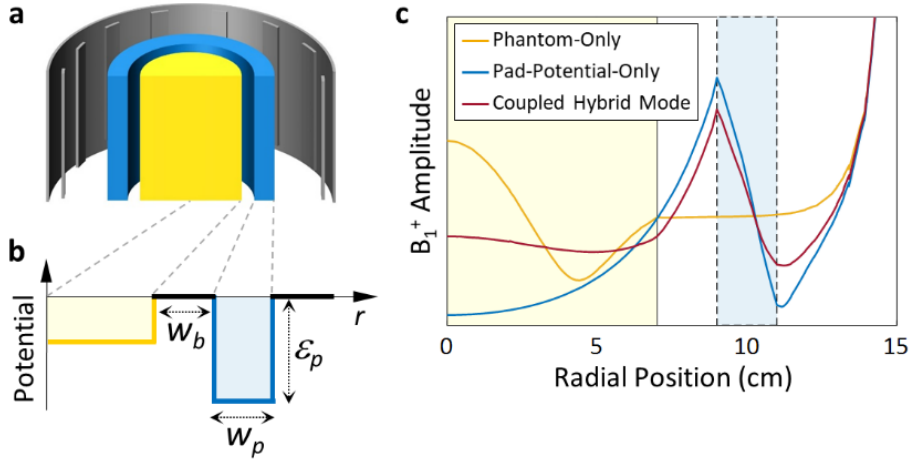


Figure 3.2.1 | The concept of evanescent mode coupling for MRI B_1^+ shimming with the pad potential. (a) Schematic of the proposed MRI B_1^+ shimming system: RF coil (gray), phantom (yellow), and cylindrical pad (blue). (b) The corresponding permittivity potential layout along the radial direction: phantom (yellow), air-gap barrier (black), and pad (blue line). (c) The plot of the B_1^+ field amplitude along the radial direction at the center of the axial plane ($z = 0$): phantom-only (yellow curve), pad-potential-only (blue curve), and both the phantom and pad potentials (red curve). The yellow- and blue-shaded region each corresponds to the brain phantom and pad.

3.3 Optimization process

While some clinical imaging prefer B_1^+ profiles brighter in the central region of the ROI, a flattened mode profile is preferred in conventional, 2D MRI scanning. Here, focusing on the 2D homogenization of B_1^+ over the transverse plane, in terms of the control parameter set (d_p, w_p, w_b) , we look into the following figures of merit (FOMs):

1. B_1^+ maximum-to-minimum ratio (MmR) over the axial plane (r, θ) signifying the degree of 2D flattening;
2. The position of the B_1^+ node in the radial direction (r_{node}) representing the redistribution of the B_1^+ fields;
3. The contour of B_1^+ at the plane (r, z) showing homogenization over the z -direction.

Figure 3.3.1 shows the effect of the pad potential-well depth d_p on the mode profile of the phantom. When the pad potential is shallower than that of the phantom ($\epsilon_p < 80$) (Figure 3.3.1 a,b), the effect of the pad on the mode shaping is not significant, with the deeper and wider potential of the phantom dominating the coupled system. On the other hand, with a pad permittivity $\epsilon_p > 200$ (Figure 3.3.1 h,i), the B_1^+ field is strongly confined in the pad, inhibiting its coupling to the phantom. At fixed $w_b = 2$ cm and $w_p =$

2 cm, with $\varepsilon_p = 180$, the lowest axial MmR of 1.2 is obtained, far lower than the MmR of 4.3 for the phantom-only case ($\varepsilon_p = 1$).

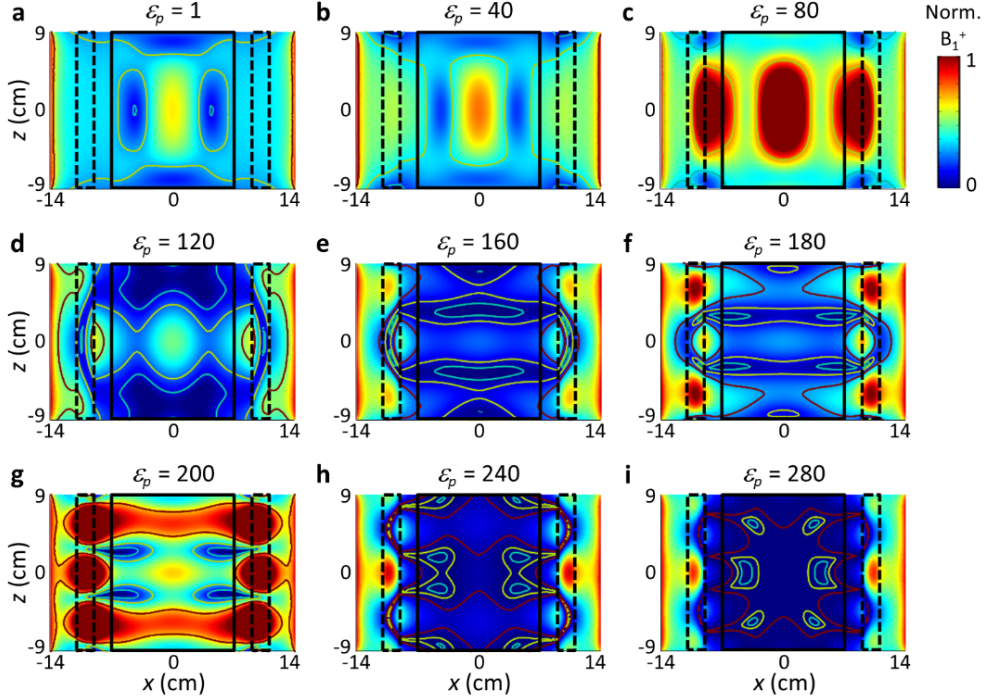


Figure 3.3.1 | Effects of the pad permittivity ε_p (pad potential depth) on the mode shaping. Normalized field amplitude in the sagittal plane ($\theta = 0$). Contour lines represent the $B_1^+ / B_1^+_{center}$ values of 1 (red), 1/2 (yellow), and 1/4 (blue). The region of interest, i.e., the cylinder phantom, is marked with a black rectangle. The pad is marked by the black-dashed rectangles. The width of the air-gap potential barrier w_b is set at 2 cm. The width of the pad potential well w_p is set at = 2 cm.

It is noted that resonant condition is satisfied at around $\varepsilon_p = 80$ and $\varepsilon_p = 200$, showing high field confinement and field pattern of the standing wave along the z -axis. On the other hand, a more uniform radial field pattern is formed at $\varepsilon_p = 180$, not $\varepsilon_p = 200$ which is the resonant point with typical field distribution, because of boundary condition with more uniform periodicity, signifying why we need to consider the pattern of evanescent coupling as well as field pattern inside the pad potential. While details for the effects of evanescent coupling pattern on the mode-shaping will be discussed in the following, it is noted here that this pattern dependency shows the signature of the mode-shaping effect of 3D structure, not 2D, which we need to consider.

To clarify the effect of the auxiliary pad potential well on the mode-shaping, it is helpful to compare the mode-shaping cases to the corresponding pad-potential-only cases. Figure 3.3.2 g-i depicts the effects of the pad potential depth on the mode profile, especially inside the cylindrical pad, for the pad-potential-only cases. Figure 3.3.2 also says, in a qualitative manner, why the B_1^+ field in the pad with excessively deeper potential is hard to be coupled to the phantom and why only a few modes are excited in the phantom while higher modes can be supported in the pad. In the phantom-pad-coupled system, higher-order mode corresponds to the higher eigenvalue k_z , associated with the lower-level energy E (closer to the pad potential level). For the case of the pad with finite thickness, k_ρ of the wave inside the pad potential is upper bounded for forming a guided mode, and then

corresponding $(E - V) \sim (k^2 - k_z^2)$ is also upper bounded. By increasing the permittivity of the pad related to the decrease of the pad potential, corresponding energy (negatively proportional to the square of k_z) also becomes lower, and in certain values of pad index, the mode dominated by the pad has an energy level lower than the potential of the phantom. Thus, the coupling between the modes of the pad and the phantom with the same energy is prohibited, failing to form a corresponding super-mode, which is not beneficial to the phantom mode shaping. Fundamentally, for the wave inside the phantom with the fixed value of k determined by the index of the phantom, k_z is also upper bounded by the dimension of the phantom, implying only a few modes are involved in the field distribution in the phantom.

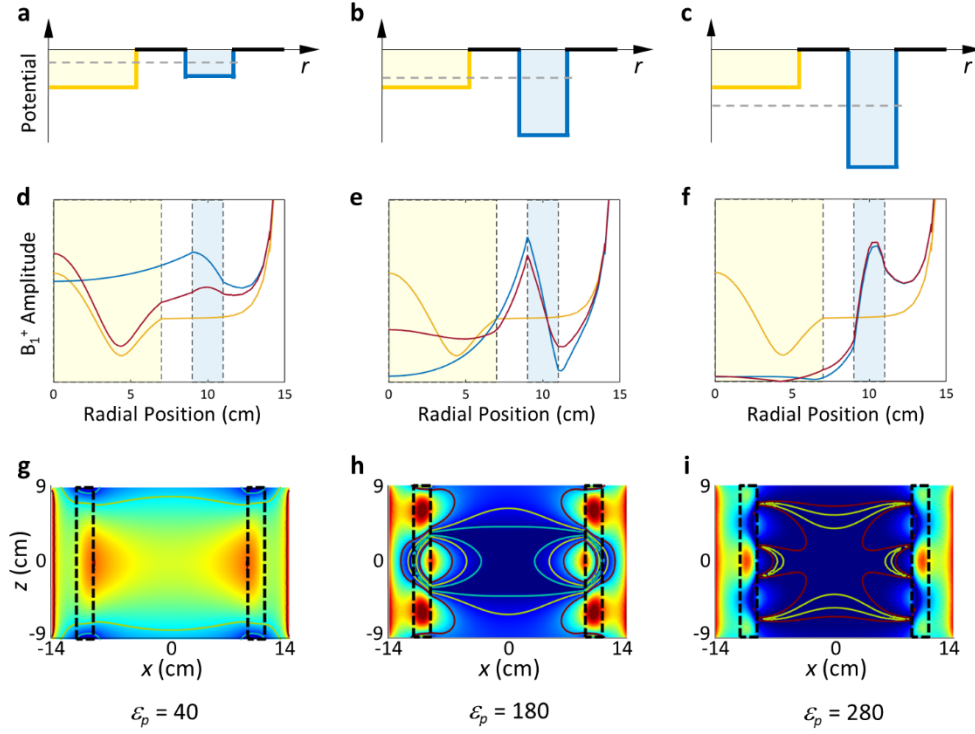


Figure 3.3.2 | Coupling of the potential well for various pad potential depth. (left column) Phantom potential well dominant system ($\epsilon_p = 40$). (center column) Pad potential well dominant system ($\epsilon_p = 180$). (right column) Much deeper pad potential system ($\epsilon_p = 280$). Higher-order mode coupling is failed. (upper row) The permittivity potential layout along the radial direction. The eigenvalue of the dominant mode is marked with the gray dashed line. (middle row) B_1^+ field amplitude along the radial direction at the center of the axial plane ($z = 0$). phantom-only (yellow curve), pad-potential-only (blue curve), coupled-system (red curve). (lower row) Normalized field amplitude in the sagittal plane for pad-potential-only cases.

Figure 3.3.3 shows the effect of the pad width w_p at various ϵ_p . As expected, the depth and width of the potential operate in a complementary manner providing almost the same pattern of modes and MmR values, e.g., for sets $(\epsilon_p, w_p) = (140, 3 \text{ cm})$, $(180, 2 \text{ cm})$, and $(300, 1 \text{ cm})$, implying an extra degree of freedom in the selection of pad materials (Figure 3.3.3 b). For the pad potential sufficiently thin to support only a single mode, increasing the thickness of the pad potential leads to a decrease of the radial wavenumber k_ρ inside the pad. In this case, for the same value of k_z , k and corresponding ϵ_p must be a lower value than those for the thinner potential case (Figure 3.3.3 b,c). It is also noted that the lowest MmR is achieved when the node positions are farthest from the center, signifying the redistribution of the B_1^+ fields in the radial direction for the shimming.

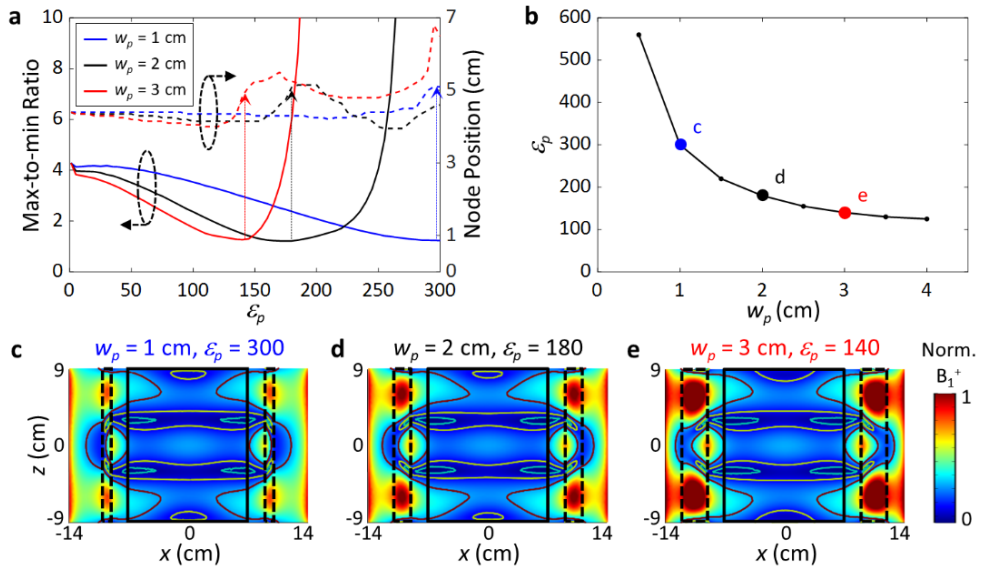


Figure 3.3.3 | Effects of the pad potential width w_p on the mode shaping.

(a) Max/min ratio (left axis, solid curves) and node position (right axis, dotted curves) obtained for various w_p (1~3 cm), at the central plane of the ROI ($z = 0$). (b) Relation between w_p and ε_p , obtained for the minimum MmR = 1.2. (c-e) Mode profile in the sagittal plane ($\theta = 0$). Potential barrier width $w_b = 2$ cm.

Figure 3.3.4 shows the effects of the air-gap barrier width w_b on the mode shaping. It is noted that $w_b = 0$ refers to a pad in contact with the phantom, and $w_b > 0$ corresponds to the evanescently coupled potential case. By controlling w_b , it is possible to adjust the strength of the evanescent coupling from the high-permittivity pad while retaining the general shape of the pad mode. From this added degree of freedom, we find that a nonzero w_b consistently provides much better homogeneity than the contact pad ($w_b = 0$), which has been demonstrated previously [86, 87, 88, 108, 109]. An MmR value of 1.2 is obtained, far lower than that in the case of the contact pad (MmR $> \sim 2.6$). Furthermore, we note that the stability of our solution against a range of w_b values implies the robustness of our evanescent mode-shaping solution to the shape or displacement of the used phantom. In the optimization process, only three factors (effectively two) need to be considered for homogenization, which is less complex than the pad optimization scheme in other studies [94, 95].

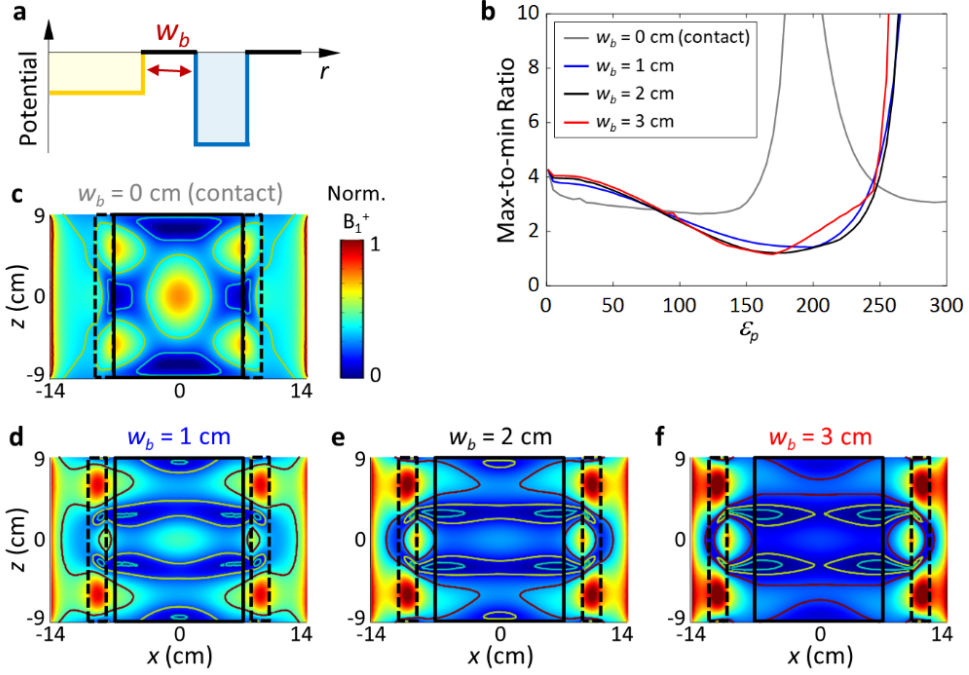


Figure 3.3.4 | Effects of the air-gap potential barrier width w_b on the mode.

(a) Potential distribution in the radial direction. (b) Max/min ratio obtained for various w_b values at the central plane of the system ($z = 0$). (c-f) Mode profile in the sagittal plane ($\theta = 0$). $\epsilon_p = 180$, and $w_p = 2$ cm.

Figure 3.3.5 shows how the contact pad depth affects the mode shaping. As mentioned above, by the contact-based potential, it is hard to obtain the shape of the mode in the form of maximizing the transversal 2D homogenization, restricting the field flattening effect. For exciting the higher-order phantom mode, it is necessary that the pad potential dominate the system with a large value of k_z and small value of the corresponding k_ρ . In

the directly coupled potential, wave in the pad potential well feels the decreased potential barrier between the phantom and the pad potential, not the potential barrier but step potential, speaking more rigorously, and then k_p no longer sustains that sufficiently reduced value.

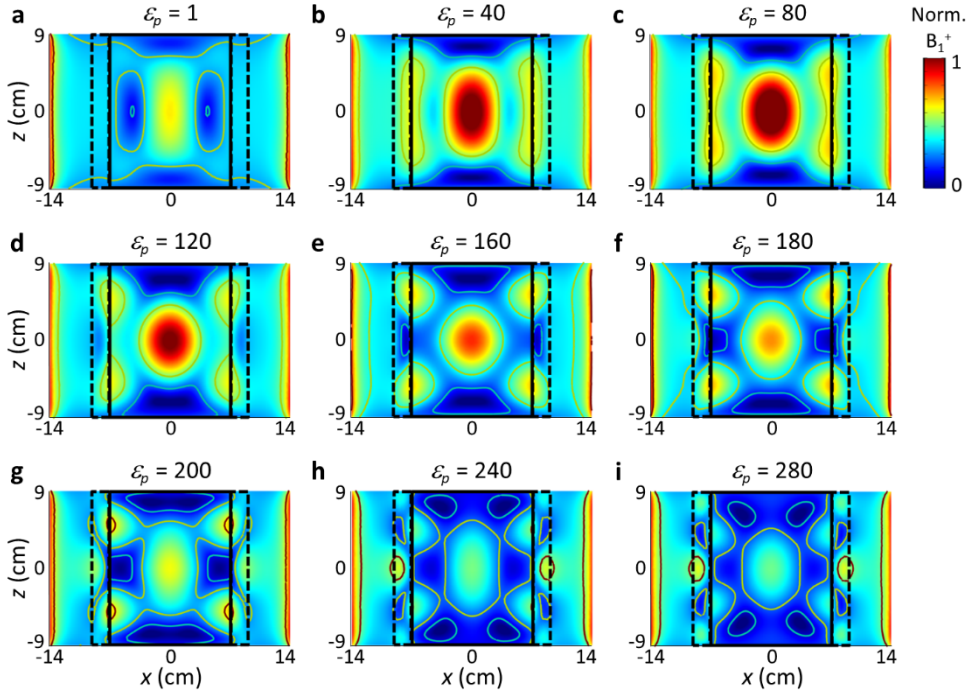


Figure 3.3.5 | Effects of the pad potential depth on the mode shaping for contact pad case. Mode flattening effect in the contact potential case is not significant in comparison to that in the evanescently coupled potential case.

3.4 Effect of the phantom and pad geometry and other material parameters of the pad.

By replacing the cylindrical phantom with a more realistic one of prolate spheroid geometry (semiaxis of 7 cm along the x -direction, 7 cm along the y -direction, and 9 cm along the z -direction), we continue the optimization of the pad geometry for 2D scanning MRI. It is found that the B_1^+ mode profile is not critically sensitive to the geometry of the tested phantoms unless the size of a phantom changes dramatically. Especially when the pad mode dominates the overall system with a high pad-permittivity value, the geometry of the phantom is perturbative only to the overall system behavior. Considering that the homogeneity of the B_1^+ field over a sliced plane affects the performance of the 2D scanning MRI system, we focus on the in-slice B_1^+ uniformities of the system. Figure 3.4.1 shows MmR values and mode profiles along different z -cut planes without and with the mode-shaping pad. It is noted that the two nodes of B_1^+ at $z \sim \pm 3$ cm are the signatures of the Fabry-Perot resonance modes of the high-permittivity pad along the z -direction. Overall, the max/min ratio of B_1^+ in a transverse plane is kept less than 2 throughout the phantom. Specifically, with the cylindrical pad, a large reduction (max of 57%) of the MmR is observed in the central region ($z = -4 \sim 4$ cm) of the spheroid phantom, where B_1^+ field focusing is usually observed without the application of an evanescently coupled pad.

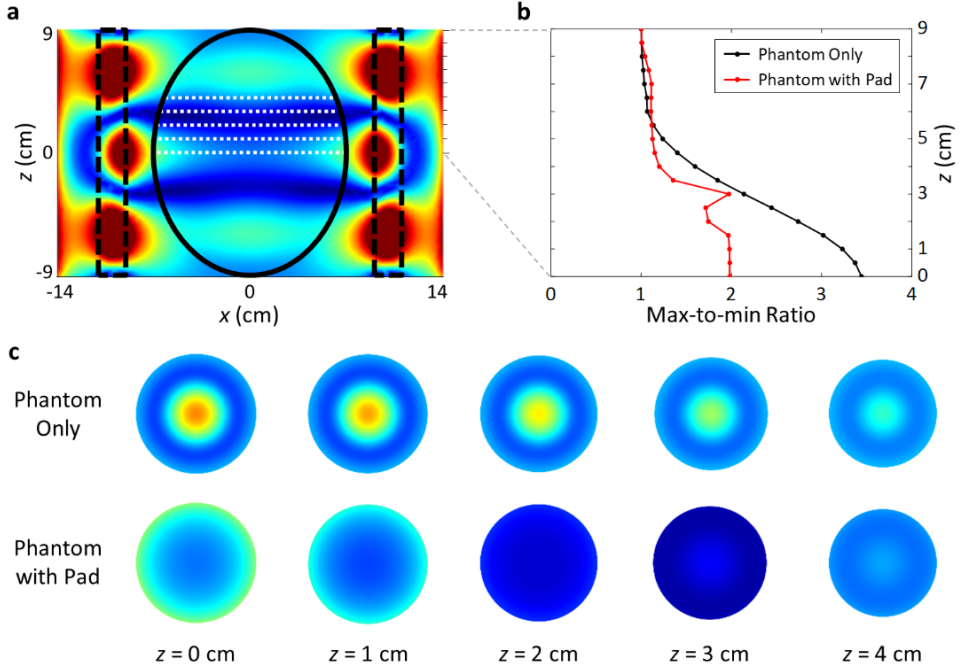


Figure 3.4.1 | B_1^+ homogenization tested with a spheroidal phantom (long axis = 9 cm, short axis = 7 cm). For the pad, $\epsilon_p = 188$, $w_b = 2$ cm, and $w_p = 2$ cm. **(a)** Mode profile in the sagittal view. **(b)** Max/min ratio at different axial slices (z-positions). **(c)** Axial images along the z-direction.

As mentioned before, the evanescent coupling strength between two potential wells is one of the main factors determining the field pattern inside the target phantom. As an example to show this effect explicitly and make use of its efficiency, a potential well composed of a curved cylindrical pad structure with matched gap size between the boundaries of the spheroidal phantom and the curved pad is applied. In these configurations, the coupling between two potential wells is more conformal and uniform to shape the field

profiles more effectively. Figure 3.4.2 shows the effect of the curved pad potential on the mode shaping with field distribution and MmR values along z -axis slice cuts. When the pad potential dominates the system, curving the geometry of the cylindrical pad does not change the general mode shape of the pad significantly and works as a perturbation to the system, compared to the case of *straight* cylindrical pad potential with pad permittivity of $\epsilon_p = 162$. The potential pad with these additional degrees of freedom to control the coupling to the phantom allows the mode hybridization to manipulate the mode-shaping, forming a more homogeneous axial B_1^+ distribution inside the phantom in comparison to the potential pad of straight cylindrical geometry. For the whole region of the spheroidal phantom, MmR value for transverse planes is less than 1.4, far improved than the straight cylindrical pad case. This representative example demonstrates the importance of the coupling strength and hybridization pattern.

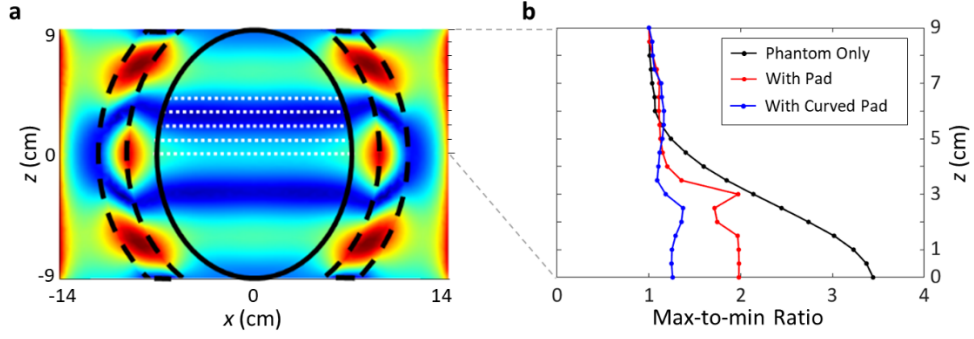


Figure 3.4.2 | B_1^+ homogenization tested with a spheroidal phantom using the gap-matched pad. For the curved pad, $\epsilon_p = 162$, $w_b = 2$ cm, and $w_p = 2$ cm. **(a)** B_1^+ field distribution in the sagittal plane. **(b)** Max/min ratio at different axial slices (z -positions). Much more homogenization is achieved by gap-matching.

In view of the refractive index, the magnetic permeability of the pad should work as an equivalent potential for the B_1^+ RF field in the same way as the electric permittivity discussed earlier. In Figure 3.4.3 a-c, as an additional degree of freedom in the design of the B_1^+ shimming pad, we present cases of magnetic pads ($\mu_p = 2$, $\epsilon_p = 135$), ($\mu_p = 4$, $\epsilon_p = 98$), and ($\mu_p = 6$, $\epsilon_p = 78$), such as those based on metamaterials, providing a similar B_1^+ RF field pattern to that of nonmagnetic pads ($\mu_p = 1$, $\epsilon_p = 180$). In Figure 3.4.3 d-f, we also show the effect of pad loss (or the imaginary part of the permittivity, σ_p) on the mode shaping. For a non-negligible damping of $\sigma_p > 0.01$, the z -directional Fabry-Perot resonance in the pad is suppressed, decreasing the

contrast or inhomogeneity of the B_1^+ field in the z -direction. Together, these results offer strategies for the selection of materials, and the pad-based 3D shimming of the B_1^+ RF field.

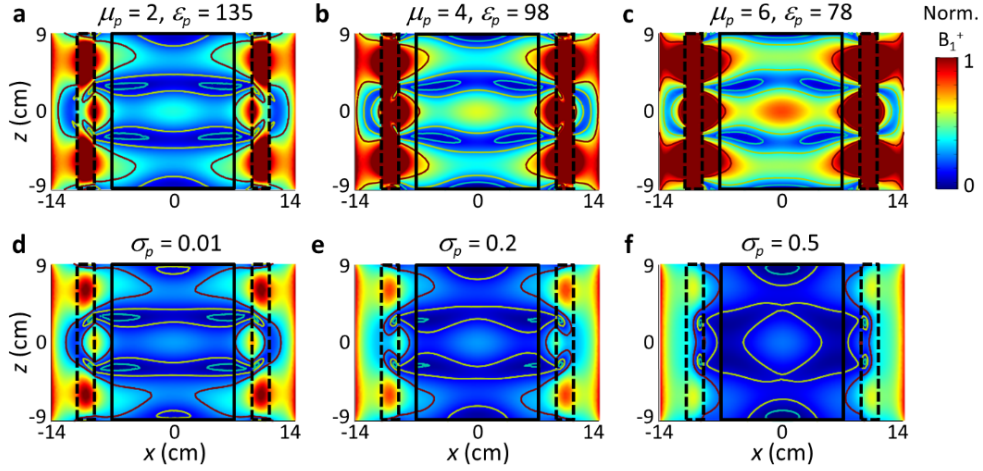


Figure 3.4.3 | Effect of the magnetic permeability and the loss of the pad.

(a-c) Mode profile for a magnetic pad of $\mu_p = 2, 4, 6$. (d-f) Effects of pad loss ($\sigma_p = 0.01, 0.2, 0.5$) on the mode shaping. $\varepsilon_p = 180$. For all cases, $w_b = 2$ cm, and $w_p = 2$ cm.

3.5 Effect of the inhomogeneous distribution of materials: human voxel model

To demonstrate that the concept of an auxiliary mode-shaping potential well can be extended to more realistic distribution of materials, a numerical experiment for mode shaping with a human voxel model is conducted. The voxel model is representatively used to mimic the geometry and material distribution of the human almost precisely, and we accept the MIDA human voxel as the specimen for MRI numerical experiment. Main electromagnetic material parameters related to obtaining an MR signal are presented in Table 3.5.1. Table 3.5.1 shows the main materials with their electromagnetic properties composing the human voxel model, and the full lists of materials are attached in Appendix A.1. Figure 3.5.1 shows the effect of the mode shaping pad on the mode profiles and the resultant MmR improvement along different z-slices. The MmR values are measured over the brain tissues of the human voxel and depicted over $z > 0$, where the field inhomogeneity mainly originates. With the mode shaping solution, the MmR values are reduced by 27% on average in comparison to those in the case without the pad, and a reduction of MmR is maximized in the central region of the human voxel (max 53%). As mentioned before, the loaded voxel and corresponding potential well of which permittivity and conductivity less than those of phantom does not significantly perturb the pad potential dominating system.

A numerical experiment is performed with a commercial simulation program of the CST studio suite, which is available to conduct electromagnetic simulation for the human voxel family. Due to the asymmetric geometry of the voxel model, a little but not a significant modification of the geometry of the MRI system is done. RF coil system is expanded to a little larger dimension: the radius of coils is 17 cm, the radius of the shield is 19 cm, and the height of coils and shield is 24 cm. Surface current sources modeling the excitation coil are replaced with line current sources with the same excitation condition of amplitude and phase evolution.

Material name	Relative permittivity	Conductivity [S/m]
Blood Vessel	48.3	0.537
Brain Gray Matter	60	0.692
Brain White Matter	43.8	0.413
Brainstem	59.7	0.973
Cerebellum Gray Matter	52.72	0.942
Cerebellum White Matter	43.8	0.413
Cranial Nerve	36.9	0.418
CSF	72.7	2.22
Epidermis/Dermis	49.8	0.641
Dura	48	0.804
Hippocampus	60	0.692
Hypothalamus	60	0.692
Muscle	58.2	0.771
Parotid Gland	78	0.716
Skull	13.4	0.0872
Spinal Cord	36.9	0.418
Tendon	48	0.537
Thalamus	60	0.692
Tongue	58.9	0.745

Table 3.5.1 | Electromagnetic properties of main materials composing the human voxel model MIDA. Tissues of the brain are highlighted with yellow shade, which constitutes the ROI for assessing the B_1^+ homogenization.

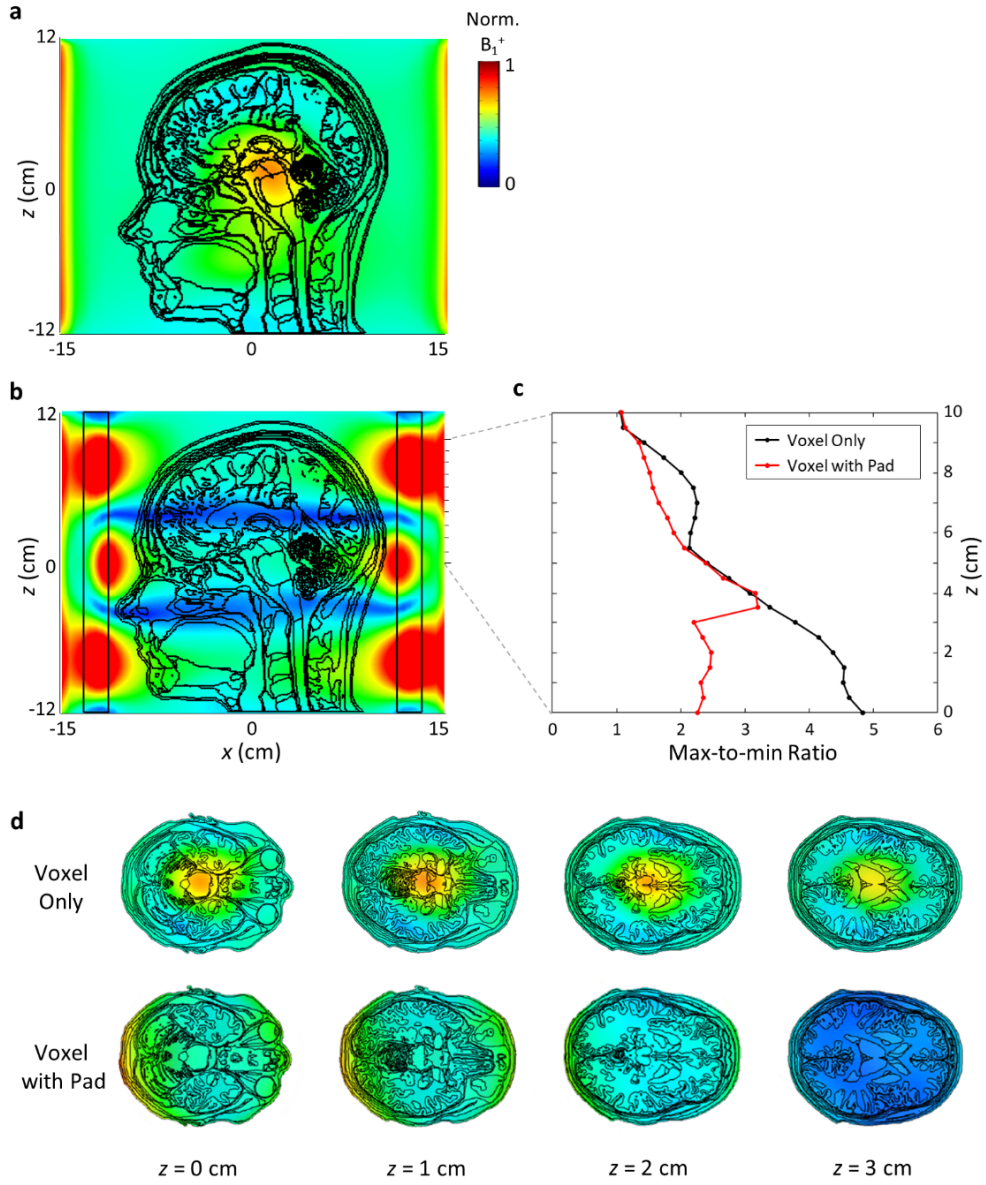


Figure 3.5.1 | B_1^+ homogenization tested with a human head voxel model, MIDA. (a) Sagittal image without mode shaping pad potential. Central brightening is observed. (b) Modal profile with the mode shaping pad in the sagittal view. For the pad, $\varepsilon_p = 131.5$, and $w_p = 2$ cm. w_b is not strictly defined, unlike for the phantom case, due to the asymmetric geometry of the voxel

model. The inner radius of the cylindrical pad is set at 11.5 cm, and the height of the cylindrical pad is 24 cm. **(c)** Max-to-min ratio value as the figure of merit at different axial slices. It is noted that axial slice is defined in $z = 0$ cm to $z = 10$ cm. **(d)** Axial images corresponding to the z -cuts.

3.6 Effect of the mode shaping potential pad on the SAR distributions

In the application of the mode-shaping solution to the MRI system, the effect of the potential pad on the distribution of the electric field as well as the magnetic field in the human body needs to be addressed. Related to the safety issue, the effects are assessed by a heating reaction inside the human body caused by electromagnetic waves radiated from the RF excitation coils of the MRI system. Quantitatively, by introducing the specific absorption rate (SAR) concept, the amount of the electromagnetic energy absorbed in a certain mass of tissues (typically 1g, 10g, or 1kg) during an MRI scan for image acquisition is measured in the unit of W/kg. The Food and Drug Administration (FDA) and the International Electrotechnical Commission (IEC) recommend the SAR values not to exceed the limits set by different levels depending on the target body part.

To verify that the proposed mode-shaping potential pad satisfies the safety regulations, the SAR values (10g) are calculated. The SAR values are quantified by employing the process that Vaidya et al. explained in their paper [110, 111]; the average of B_1^+ in the ROI is scaled to apply rectangular pulses with 2 ms duration for both 90° and 180° flip angle, and the scaled B_1^+ is squared to scale the SAR. Then, this SAR is scaled to correspond to a certain pulse sequences, and for our cases, the turbo spin-echo (TSE) sequence with

TR = 6000 ms, ETL = 16 is used. In setting the region including all brain tissues except the node region ($z = -4 \text{ cm} \sim -3 \text{ cm}$ and $z = 3 \text{ cm} \sim 4 \text{ cm}$) to the ROI to be scanned, the distribution of SAR is illustrated in Figure 3.6.1. Compared to the voxel-only case, the voxel with the mode shaping pad reduces the maximum local SAR (0.85 W/kg to 0.58 W/kg) and the average SAR (0.24 W/kg to 0.13 W/kg) and modifies SAR distributions (depressed in the central region, shifted to the periphery). For scanning the node region, due to the lower average field amplitude compared to the other region, the resultant SAR values should be increased by a factor of 8.6. Even in that case, the maximum local SAR (5.01 W/kg) and the head average SAR (1.12 W/kg) are well below the suggested SAR limits (maximum local SAR: 10 W/kg, head average SAR: 3.2 W/kg) [112, 113].

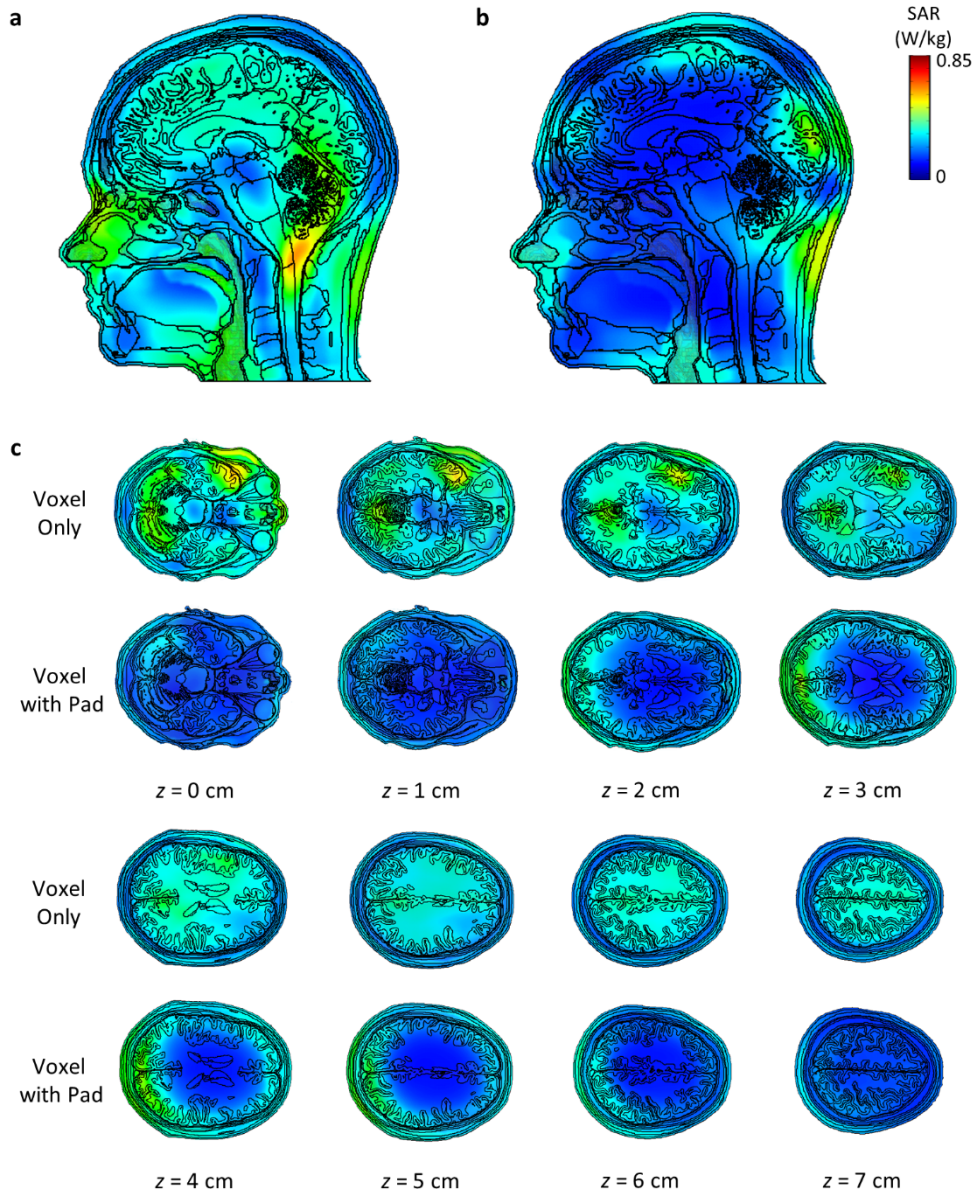


Figure 3.6.1 | Effect of the mode shaping potential pad on the SAR distributions. SAR distributions in the sagittal plane for the case of (a) MIDA voxel only and (b) MIDA voxel with the mode shaping pads. (c) SAR images at different axial cuts for each case. The SAR values are calculated for the ROI except for the node region ($z = -4 \text{ cm} \sim -3 \text{ cm}$ and $z = 3 \text{ cm} \sim 4 \text{ cm}$), and for scanning the node region, SAR values should be scaled by a factor of 8.6.

3.7 Robustness and stability of the mode shaping solution

For the clinical application of the mode-shaping solution to the MRI system, the different conditions of the patient should be considered. These include the variations in the human subjects' position or geometry, which could affect the mode shaping and the resulting B_1^+ field profiles. To evaluate the robustness of the mode shaping and the homogenization of B_1^+ field against these variations, tests are conducted for four representative cases: forward, backward, and lateral bending of the head (10°), and reduced volume of the head (10%). Figure 3.7.1 illustrates the mode shaping and the average reduction of the MmR for four cases of variations, compared to those for the neutral case without variation of position or geometry. For all cases, the capability to shape the mode and improve the homogeneity of the B_1^+ field keeps valid, and the difference in the average reduction of the MmR between cases is less than 4%. The MmR reduction of more than 23% can be obtained for all the cases of variations.

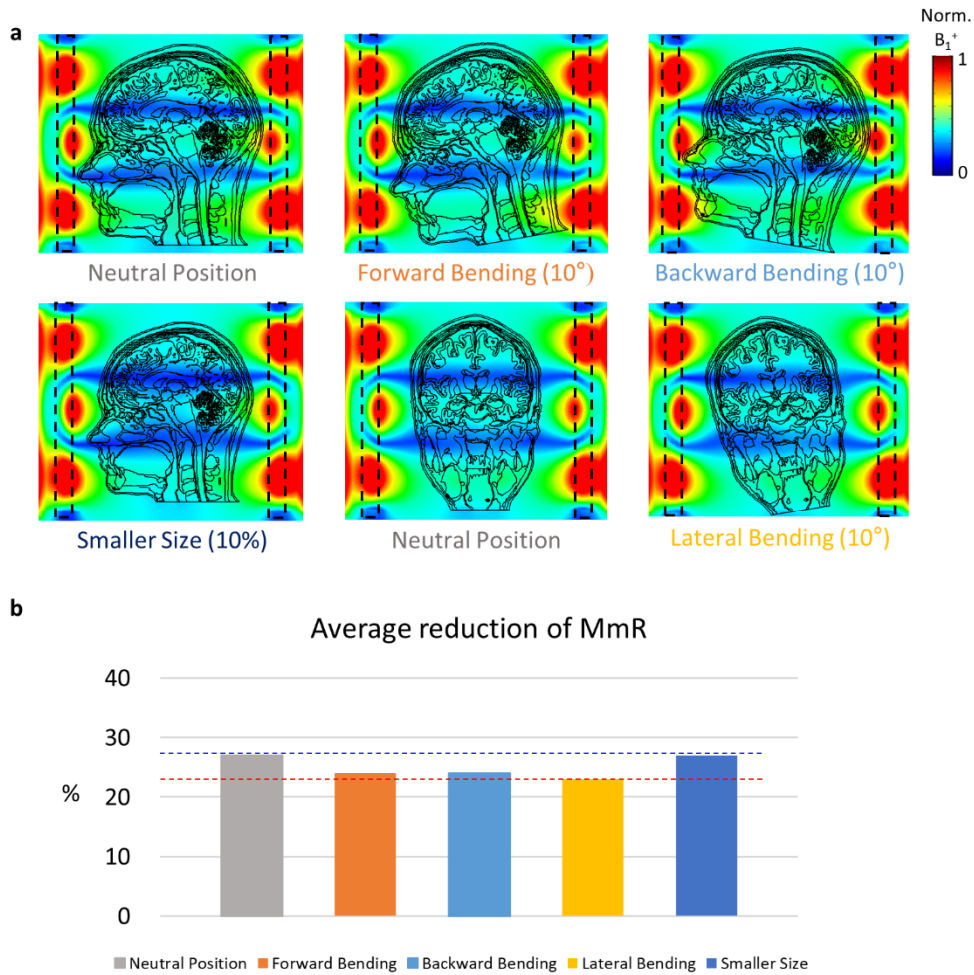


Figure 3.7.1 | Robustness or stability of the mode shaping and the B_1^+ homogenization. (a) Robustness or stability of the mode shaping solution tested against the variations in the geometry (volume reduction by 10%) and position (forward, backward, and lateral bending by 10°) of the human head. (b) The average reduction of MmR corresponding to the four variations. The maximum and minimum levels are marked with a blue dashed line and a red dashed line, respectively.

3.8 Conclusion

To summarize, we propose the concept of B_1^+ field mode shaping in the notion of evanescent coupling of an auxiliary potential to address the issue of transmit RF (B_1^+) inhomogeneity in UHF MRI. Specifically, treating the head-air-HPM (high-permittivity materials) MRI system as an RF waveguide excited by an external electromagnetic source, we systematically optimize the material and geometrical parameters of the HPM and evanescent coupling for B_1^+ shimming and prove its validity against the conventional contact-pad structure. It is revealed that the mode shape and homogeneity inside the phantom are determined by two key factors: the mode shape inside the pad potential and the hybridization strength between the phantom and the pad potentials. The mode shape inside the pad potential is again dictated by the electric permittivity of the pad (ϵ_p), the width of the pad (w_p), the magnetic permeability of the pad (μ_p), and the loss of the pad (σ_p). The hybridization strength is controlled by the width of the air potential (w_b), working as a potential barrier between the phantom and pad potentials. With the strong boundary condition derived from the high permittivity of the pad ($\epsilon_{pad} \gg \epsilon_{phantom}$), we achieve a robust, global homogenization of axial B_1^+ throughout the ROI with negligible dependence on the geometry of the phantom. With a simplified phantom of spheroidal geometry, the max-to-min ratio of B_1^+ was kept < 2 over the whole region, being applicable to 2D MRI scanning. For

scanning targets with noncylindrical geometry, more improvement of homogeneity can be achieved by matching the gap distance between the pad and target. With the robustness of the mode shaping solution, the concept can be expanded to the homogenization of the B_1^+ field for a realistic human voxel model. With the use of additional parameters, such as a noncylindrical pad geometry, an anisotropic HPM material and a metasurface HPM, further extension of our proposal should be possible for higher-level B_1^+ mode control in UHF MRI.

Chapter 4

Hybrid mode shaping with auxiliary EM potential for global 3D homogenization

In this chapter, we expand the concept of mode shaping with auxiliary potential well to address global 3D homogenization of the B_1^+ field. By manipulating the spatial distribution of potential, the shape of the dominant potential mode and the hybridization pattern with the brain potential can be controlled in a more general manner, giving a chance to achieve the mode shaping for the globally uniform B_1^+ field distribution. With control of the node formed inside the brain area, we demonstrate two kinds of shaped mode induced by potential well on the sagittal axis and axially shifted cylindrical potential well.

4.1 Mode shaping for 3D MRI scanning

Although it is not conventional, attention to 3D scanning is growing and growing. Not restricted to 3D scanning, this global homogenization is also useful in conventional 2D scanning. For the 3D full scanning, the other type of phantom mode needs to be excited to utilize additional terms of mode in the mode expansion. Dominant side potential well mainly discussed in the previous chapter only couples to the higher-order phantom mode, and therefore symmetry breaking is necessary. By breaking the symmetry, we have additional degrees of freedom for exciting other types of mode and mode mixing patterns in the phantom, not obtained from the symmetric potential well mainly discussed in the previous chapter. For breaking the symmetry of the system, in this chapter, we focus on the z -axis translational symmetry breaking. Specifically, we focus on two kinds of ways to implement it; potential well on the z -axis and z -shifted side potential well.

The potential well model presented in the previous chapter is not directly valid for the symmetry breaking cases, but we need not discard the notion entirely. Perspective on the system as the dominion for the system with high index materials and coupling to the human head is still valid, as though this symmetry breaking case has a little different pattern of coupling. Thus, insights obtained from the results in the previous chapter lead us to tackle the 3D scanning in UHF MRI. The concept of auxiliary potential can be extended

to a more general configuration of geometry and coupling.

In company with symmetry breaking, a key mechanism handling the global homogeneity is indebted to node control. Resulted in the destructive interference of the wave inside the ROI, the position and strength of the node in the fundamental head mode can be controlled by mode shaping with auxiliary potential. Specifically, the strength of the node critically determines the performance of the global homogeneity, and then approaches in terms of controlling the node are straightforward and effective. In this chapter, we consider two ways to handling the node of mode; spreading strong nodes over the ROI or shifting strong nodes to outside of ROI. Each of them corresponds to the role of the potential well on the z -axis, and z -axis shifted side potential well, respectively.

4.2 Hat pad potential for lower-order mode excitation

Another mode of lower order also allows the field homogenization by manifested in the mode expansion, and this mode gives a chance to global homogenization of B_1^+ field all over the phantom region. Specifically, the lower phantom mode has a lower axial k value and corresponding higher radial k value in comparison to those of the fundamental phantom mode. From this additional phantom mode shape, the field in the phantom can be redistributed in the form that the interference field pattern is blurred to a certain degree, especially for the radial node, which is the most critical reason for the field inhomogeneity.

Insights from the previous chapter say when potential outside the phantom dominates the system, the mode profile of the system is approximately governed by the mode of the external potential. Thus, we apply the auxiliary potential of which mode has a higher radial wavenumber than that of the phantom, which is implemented with a high index disk structure on top and bottom of the phantom. Similar to the side cylinder case, when the disk ‘hat’ of high index dominates the system, the phantom-hat coupled system comes to be governed by the hat potential, where the effect of the mode shaping is shown more clearly. The structure of the hat potential system is depicted in Figure 4.2.1. The disk hat pad has a slightly larger radius

compared to that of the phantom for supporting the hat modes of the high-valued radial wavenumber more efficiently, because hat mode depends on the geometry of the hat pad.

Figure 4.2.1 shows the effect of the hat potential ε_h on the mode shaping. Additional FOM needs to assess the effect of mode-shaping on the global B_1^+ homogeneity, and for this reason, we add the global max-to-min ratio (GMmR) defined over the whole brain region to the FOM lists. Auxiliary potential on the top and the bottom of the phantom naturally induces the mode shape pulled along the axial direction, which is directly related to the k_z of the phantom mode, improving the field uniformity in the axial direction. Simultaneously, a strong node positioned in the central region, which is the main cause of field inhomogeneity, is also spread out over the phantom and becomes diminished, leading to uniform field distribution. It is natural that the resultant shape of the mode has a radial node position shifted toward the center of the phantom, indicating that the lower-order mode is excited. By this strategy, an improved GMmR of 2.84 can be obtained at $\varepsilon_h = 300$, which is the increase of the homogeneity by 32% (GMmR for the cylindrical phantom only case is 4.19).

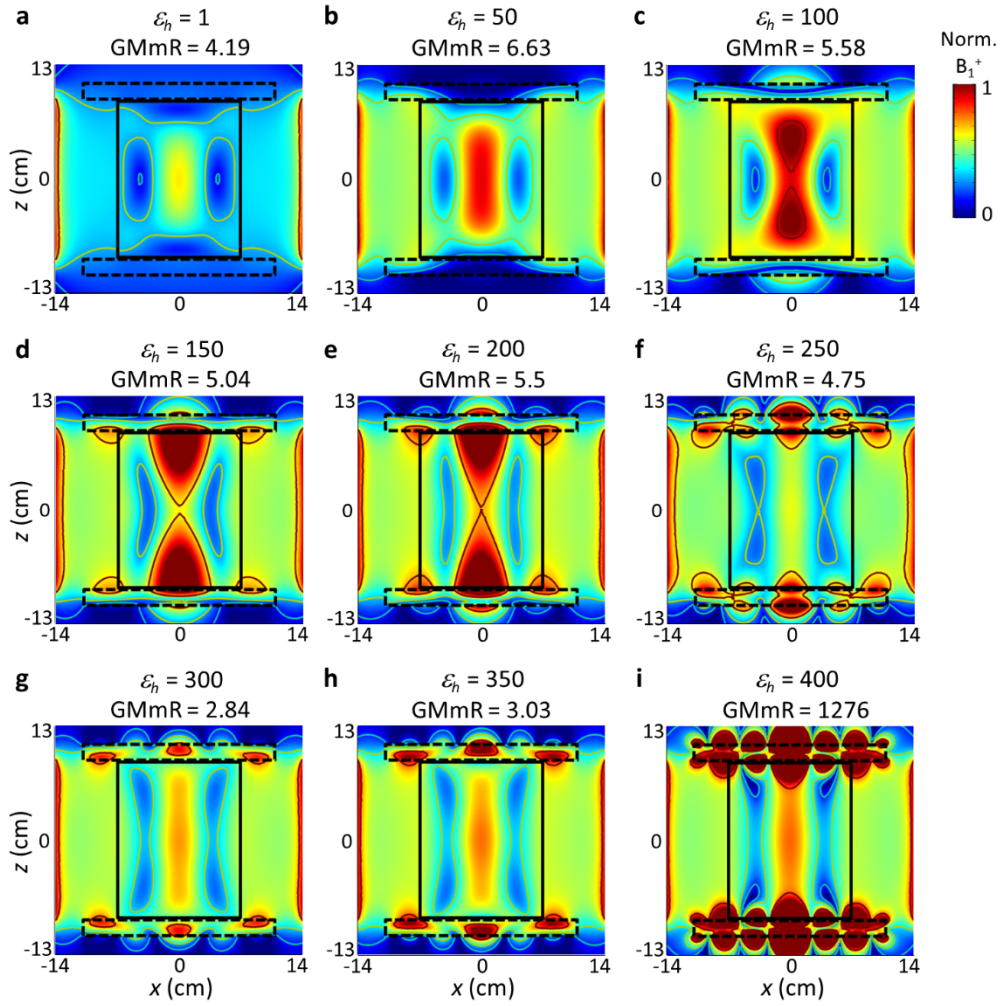


Figure 4.2.1 | Effects of the hat pad permittivity ϵ_h (pad potential depth) on the mode shaping. The hat pads are composed of two circular dielectric disks with 11 cm radius and 2 cm height, located on the top and bottom of the cylindrical phantom.

Utilizing this hat potential concept in MRI applications, a small modification of their structure is required, for the closed structure of the lower hat on the bottom of the phantom is somewhat unrealistic. This issue can be simply solved by replacing the original closed pad structure with a ring-like pad of higher permittivity (ϵ_n) with room for the neck of a human. This kind of modification performs almost equivalent mode shaping and little changes the field pattern excited by the original lower hat solution. This mode shaping with a hat-and-necklace pad potential is illustrated in Figure 4.2.2 (bottom row).

The other modification is about the geometry of the phantom, to be tested with a more realistic phantom of spheroidal shape. By bending the straight hat potential pad to match the curvature of the spheroidal phantom in the contact region on the top and bottom, we can adjust the mode coupling pattern between the auxiliary hat pad and the phantom to the geometry of the spheroidal phantom while keeping the general mode shape of the hat pad. In this potential configuration and corresponding mode coupling, we can retain similar conditions with those of the flat straight hat and the cylindrical phantom system. Figure 4.2.2 b shows the mode shaping with the curved hat potential and GMmR achievement of 2.87 (by 16% increased homogeneity compared to that of the phantom only), which is a similar value for the cylindrical case as expected. In the same manner, mode shaping with modification of the bottom hat pad for the neck room is also tested (Figure 4.2.2 d).

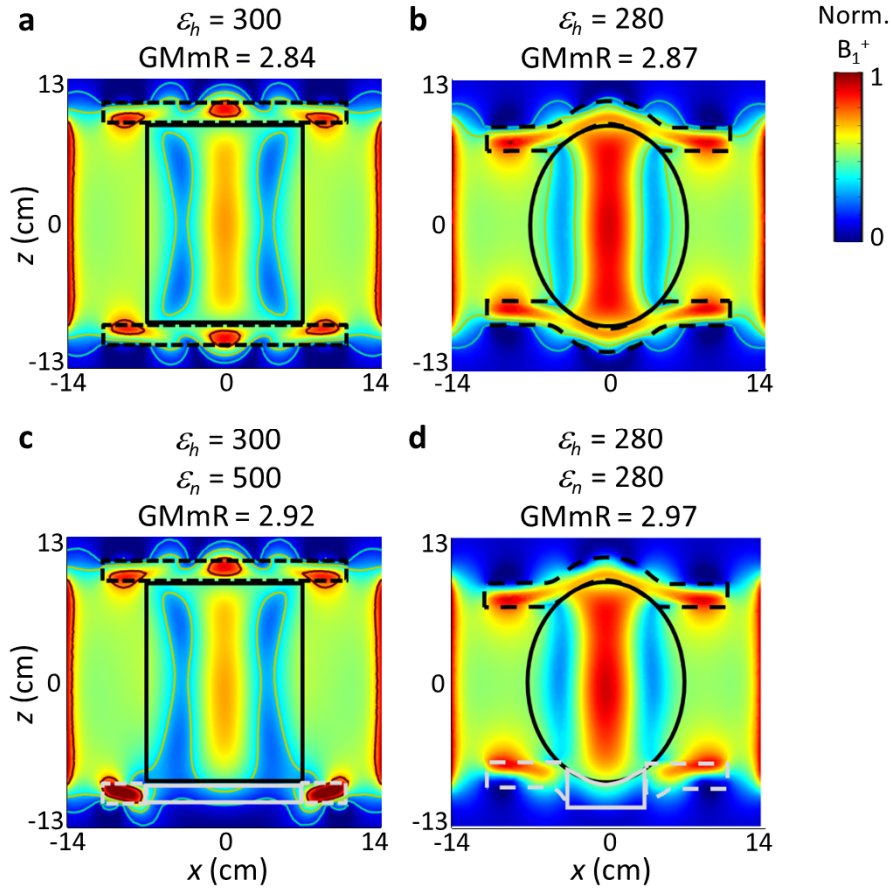


Figure 4.2.2 | Mode shaping with hat and necklace pad potential for the cylindrical and the spheroidal phantom. Symmetric hat potential on the top and bottom of the phantoms (top row) and asymmetric hat-necklace potential (bottom row) are applied. For asymmetric cases, the neck is composed of the same phantom material, and the region of it is marked with a solid gray box. The necklace pad surrounding the neck is marked with gray dashed lines.

For this kind of mode shaping, improvement of field homogeneity is basically achieved by redistribution of the mode profile in a cylindrical configuration. By cylindrical-shaped mode excitation, we can induce more improvement of global homogenization over the phantom of spheroidal geometry. The underlying mechanism exciting the lower-order mode is the same, and the configuration of the potential is set with the phantom in a dielectric cylinder can. A more feasible design is presented in Appendix B by replacing the central part of the cylinder with a spaced cylinder with the aid of the complementary relationship of the side potential. More detailed information for this mode shaping is described in Appendix B. Independent on the geometry of the phantom, a similar form of field distribution and the same value of field homogeneity can be obtained, for cylindrical phantom or spheroidal phantom of about 2.8, implying this type of mode shaping may be much beneficial for the structure having intrinsic inhomogeneity.

4.3 Asymmetric shifted pad potential

As mentioned in the previous chapters, elimination of the interference pattern of the B_1^+ field inside the ROI of the human brain is fundamentally limited by the constraint of wave properties in a single operational frequency and corresponding wavenumber. In this circumstance, it is reasonable that we select ROI, including a more critical part of the human head to scan with feasible size, and focus on the field homogenization in that ROI. We set the brain in the upper half part of the human head as ROI, for this part of ROI includes essential tissues of the human nervous system such as the cerebrum, thalamus, and cerebellum, which are the main focus of clinical attention.

In this setting, we can utilize an additional room to control the mode shaping by breaking the (z -axis) symmetry. Specifically speaking in terms of node control, by employing the tactic of pulling the strong node presented in ROI outside the ROI (forming the mode shape with a strong node outside the ROI), we can achieve a more homogeneous field profile inside the ROI. We start the discussion with the mode-shaping pad potential for B_1^+ axial homogenization, which is the main subject of the previous chapter. In this kind of mode, a spatially well-arranged node pattern with symmetry could help in showing the effect of symmetry breaking in pad potential configuration in a much clearer manner, with making the most of the mode flattening capacity, which is the original purpose of the pad potential.

Figure 4.3.1 illustrates the effects of the positional shift of the mode-shaping pad along the z -axis on the mode shaping. To show the effect of the mode shaping more clearly and directly, the dimension of the tested spheroidal phantom and RF coil system is matched similar to those of the voxel model case as in chapter 3.5; the semiaxis of the phantom along the x -direction and the y -direction is 9 cm, the semiaxis of the phantom along the z -direction is 12 cm, the radius of coils is 17 cm, the radius of the shield is 19 cm, and the height of coils and shield is 24 cm. As expected, the general mode shape inside a deep potential well by a cylindrical pad structure is not critically influenced by its position on the z -axis, and then a positional change of the potential work as an adjustment of the potential coupling and the corresponding mode hybridization pattern, which is not obtainable from the symmetric potential that is in unshifted case. Specifically, by shifting the side potential pad along the z -direction, the strong node presented in the $z = 4$ cm plane also starts to be shifted toward the same direction. To a certain point, pulling the strong node outside the ROI leads to improved field uniformity over the ROI, but too much pulling causes the new node inside the ROI, especially the upper region of ROI, to deteriorate the homogeneity again. At displacement $d_s = 9$ cm, the lowest GMmR = 2.21 over the ROI is obtained, far lower than the GMmR of 4.92 for the phantom-only case (homogeneity improved by 55%).

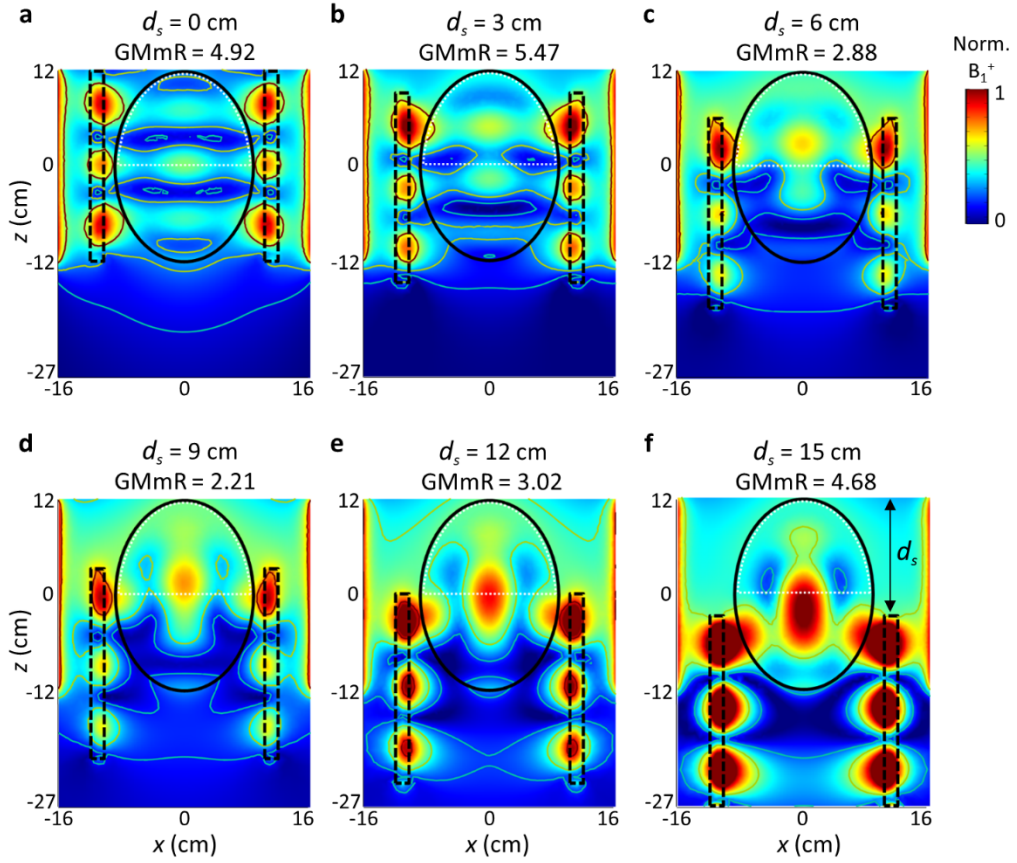


Figure 4.3.1 | Effects of the pad positional asymmetry on the mode shaping. No variance of the structure of the potential pad under positional shifting. The height of the pad is fixed at 24 cm, the width of the pad potential well w_p is set at 2 cm, and air gap width w_p is 1 cm. All the shifted potential pads have permittivity ϵ_p of 135. ROI covering the upper brain is marked with a white dotted line.

Improvement of global homogeneity for the upper half of the brain by employing the z -shifted potential obviously involves the B_1^+ field homogenization in axial slices. Even in the shifted potential, axial flattening effects by side pad potential remains on the nodal plane, and then node mainly deteriorating axial uniformity of the B_1^+ field is blurred in the ROI. Figure 4.3.2 illustrates the effect of the shifted mode shaping potential on improving the axial homogeneity of the B_1^+ field as well as the global uniformity of the field distribution. For shimming case with shifted pad, MmR values along the axial cuts over the upper half of the brain phantom keep the value under 2, which is especially useful for mitigating field inhomogeneity in the central part of the phantom (Max 50%). This case corresponds to the cylindrical pad of $\varepsilon_p = 135$ shifted by $d_s = 9$ cm.

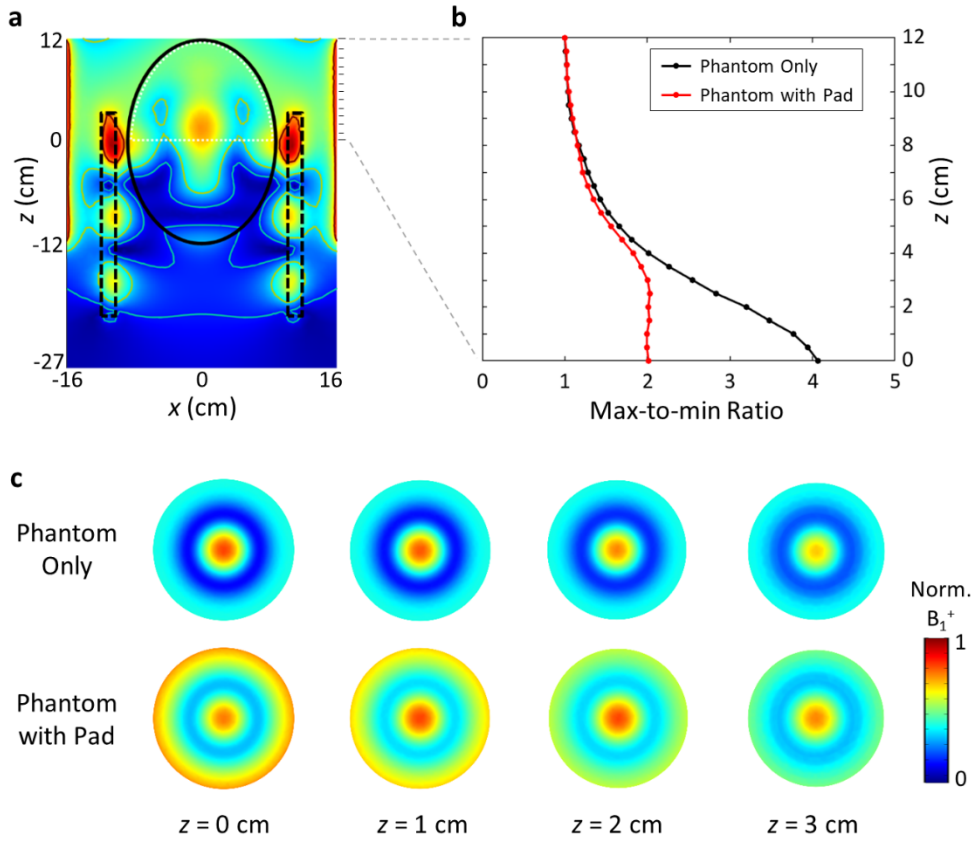


Figure 4.3.2 | Field pattern in axial slices in B_1^+ shimming by the shifted pad potential. (a) Field distribution under the shimming by the shifted potential in sagittal view. (b) MmR values over the axial slices. (c) Axial images for each slice. Normalized with the maximum B_1^+ field inside the phantom for each case.

Figure 4.3.3 shows the asymmetric shifted pad potential applied in the case of the MIDA voxel constituted of the distribution of heterogeneous materials. Similar to the voxel with employed auxiliary potential in a non-shifted position along the z -direction, when dominant potential well governs the system entirely, the effect of material inhomogeneity on the mode shaping is not very crucial. At displacement $d_s = 9$ cm, the lowest GMmR = 3.73 over the ROI of the brain in the upper half of the head is obtained, improved by 25% compared to that of the voxel only case with a value of 4.98. Furthermore, the effect of the shifted mode shaping potential on improving the axial homogeneity of the B_1^+ field as well as the global uniformity of the field distribution is still valid when the pad potential is applied to the human voxel model. For shimming case with the shifted pad, MmR values along the axial cuts over the upper half of the brain voxel keep the value under 3, and the MmR values are reduced by 20% on average compared to those of the case without the mode shaping pad. Similar to the case with phantom, the effect of the inhomogeneity mitigation is maximized in the central region of the human brain (max 40%), where the B_1^+ field nonuniformity is most severe.

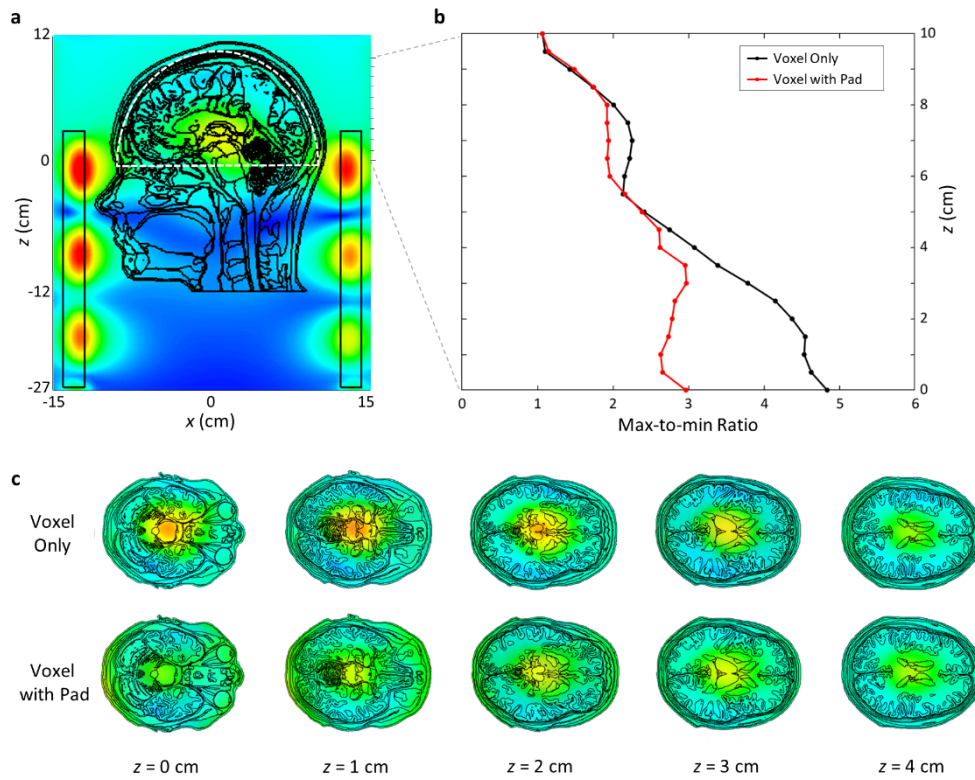


Figure 4.3.3 | Shifted asymmetric pad potential applied for B_1^+ field homogenization in the MIDA voxel case. (a) Sagittal image with a shifted asymmetric pad. **(b)** Max-to-min ratio value as the figure of merit at different axial slices. **(c)** Corresponding axial images.

4.4 Effect of the shifted potential pad on the SAR distributions

To assure that the pad solution for 3D homogenization of the B_1^+ RF field can be utilized without causing a significant heating reaction in the human subjects, the effect of the shifted potential pad on the SAR is tested. The SAR values averaged over 10 g of tissue are calculated with the same procedure in section 3.6. For the scanning of the human head, with the turbo spin-echo sequence, no remarkable changes in both the maximum local SAR (0.85 W/kg to 0.88 W/kg) and the head average SAR (0.24 W/kg to 0.22 W/kg) by the application of the asymmetric potential pad to the voxel-only system are observed. Figure 4.4.1 shows that the distribution of SAR is modified, and the reduction of SAR is remarkable, especially in the cerebrum region. Obviously, the resulting SAR values satisfy the standard suggested by FDA and IEC (maximum local SAR: 10 W/kg, head average SAR: 3.2 W/kg) [112, 113].

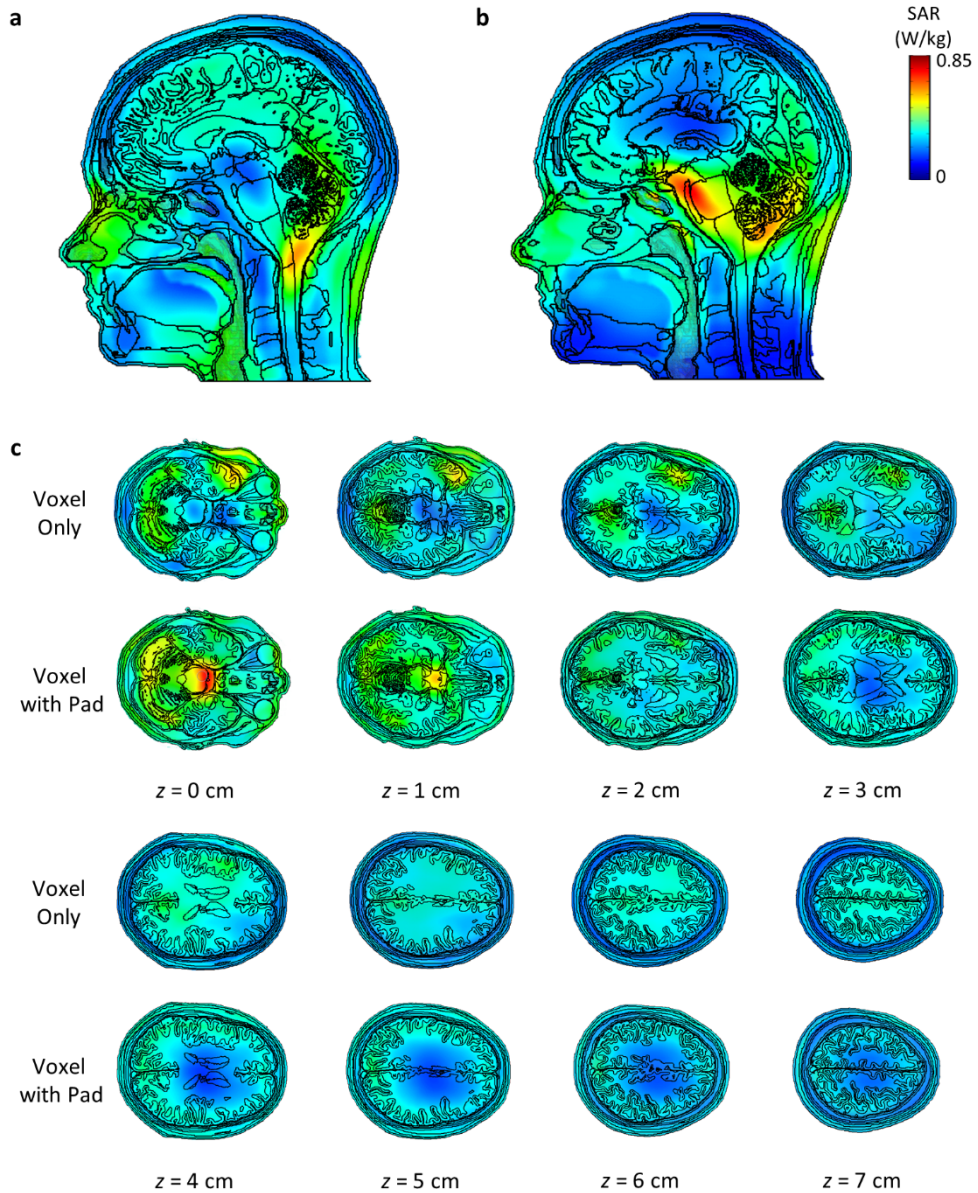


Figure 4.4.1 | SAR analysis for the human head voxel without and with the mode shaping pads. The sagittal SAR images corresponding to the turbo spin-echo sequence for the case of (a) MIDA voxel only and (b) MIDA voxel with the mode shaping pad. (c) Corresponding axial SAR images. SAR at the center of the cerebrum is depressed by the implication of the pad.

4.5 Robustness of the mode shaping with asymmetric potential pad

For the same purpose as in the 2D mode shaping solution, the robustness of the mode shaping with the asymmetric potential pad against the variations of the human head in the position and geometry needs to be checked. The robustness is tested in the three displacement variations (forward, backward, and lateral bending of the head by 10°) and the geometrical variation (reduced volume of the head by 10%), same as in the 2D case. In the case of performing the global homogenization of B_1^+ , the GMmR values, as well as the MmR values, should be considered in the evaluation of the robustness. Figure 4.5.1 depicts the effect of the variations of the human head conditions on the mode shaping and the reduction of both the MmR on average and GMmR. The ability to shape the mode and homogenize the B_1^+ field is not significantly changed under the human head in various conditions. For these conditions, the variation in the average reduction of the MmR between cases is kept less than 6%, and the MmR reduction higher than 19% can be achieved. In the GMmR reduction, the maximum difference between cases is 8%, and a reduction of more than 20% can be obtained for all the cases of variations.

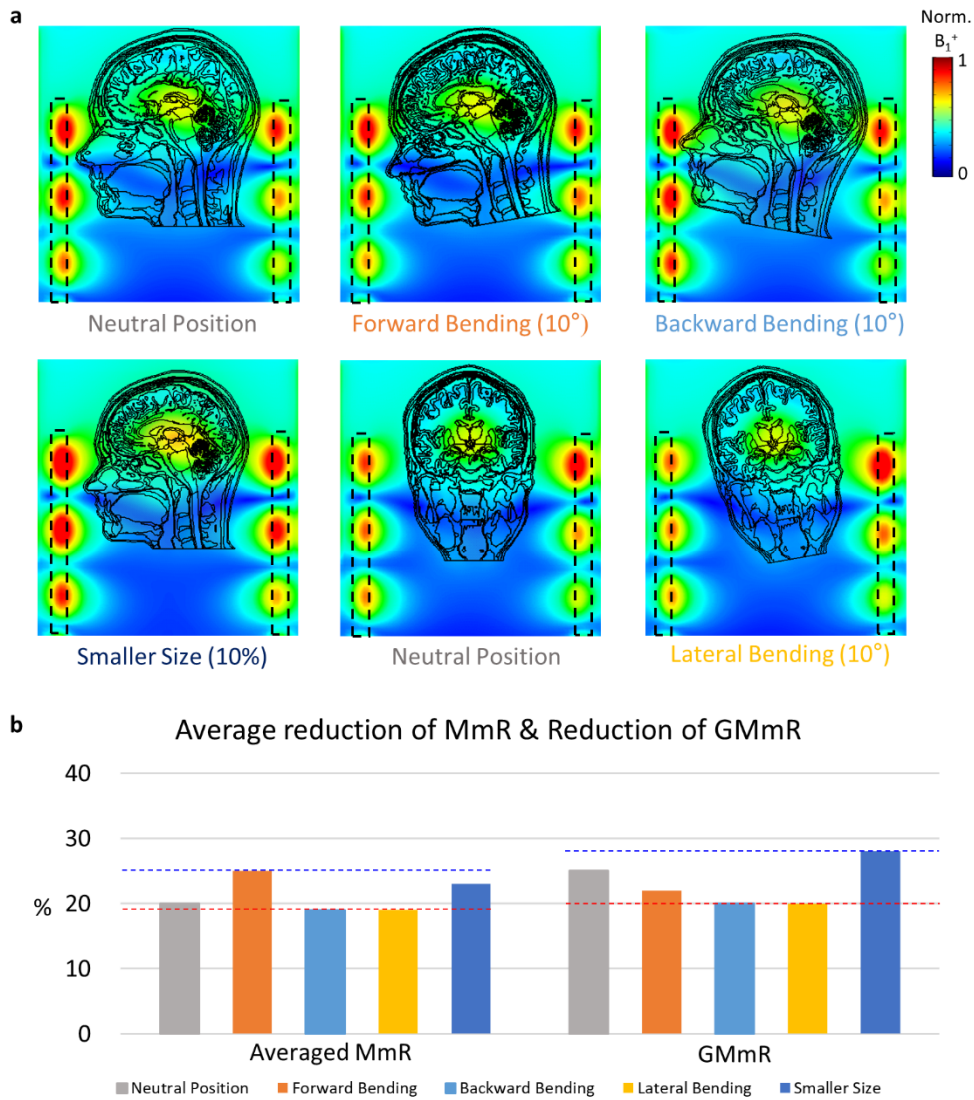


Figure 4.5.1 | Robustness of the global B_1^+ homogenization. (a) Robustness of the capacity to globally homogenize B_1^+ field against three positional variations and the geometrical variation is tested. (b) Under the variations, both averaged MmR and GMmR of the human in neutral position are changed within 5%.

4.6 Conclusion

To summarize, we expand the notion of the hybrid mode shaping with the auxiliary potential well proposed in the previous chapter to deal with the issue of B_1^+ inhomogeneity in 3D. Specifically, by utilizing the asymmetric configuration of the auxiliary potential, we introduce two kinds of mode shape suitable to improve the global homogeneity of the B_1^+ field. Potential implemented by a pair of disk pads on the top and bottom of the human head shape the head mode with lower axial wavenumber, leading to spread the strong node concentrated in the peripheral region of the head. The positional shift of the axial mode shaping potential pad along the axial direction induces the shape of the head mode with its strong node guided out of the region of interest. Both mode shaping can be applicable to achieve the global 3D homogenization of the RF B_1^+ field in UHF MRI.

Although it is necessary to shrink the ROI to some extent, a mode shaping solution with spatial shifting gives a chance to utilize the homogenization capacity more efficiently by setting the ROI according to the purpose of scanning. In this dissertation, we focus on the brain scanning by setting the upper half of the brain to the ROI.

Chapter 5

Conclusion

In this dissertation, we propose the notion of mode shaping based on the evanescent coupling of auxiliary potentials to address the issue of B_1^+ field inhomogeneity in ultra-high-field magnetic resonance imaging. With the notion of evanescently coupled potential, the effects of the auxiliary potential configuration, directly related to the geometrical and material parameters of the pad, on the mode shaping and corresponding field homogenization are investigated. From the analysis and optimization, we obtain a robust mode shaping pad solution to achieve 2D global homogenization of axial B_1^+ field for the phantom of various geometry and the realistic voxel model of heterogeneous materials, which is applicable to the conventional 2D MRI scanning. Extending the mode shaping approach with the symmetry breaking, we can control the B_1^+ mode at a higher-level to address the inhomogeneity

issue in 3D. With the additional capability to manipulate the mode shaping, we also propose a pair of disk pads on the top and bottom of the human head and an axially shifted cylindrical pad as the mode shaping solutions for 3D global homogenization of the B_1^+ field. Furthermore, to assess the practical feasibility of the mode shaping solutions, the safety and robustness analysis of the solutions are also conducted.

By providing an unconventional viewpoint and systematic guideline for the mitigation of B_1^+ inhomogeneity, this method would expand the capability of RF passive shimming in UHF MRI.

Appendix A

Supplements for Chapter 3

A.1 Material and geometry for the MIDA voxel model

Material name	Relative permittivity	Conductivity [S/m]
Adipose Tissue	11.7	0.0765
Air Internal - Ethmoidal Sinus	1	0
Air Internal - Frontal Sinus	1	0
Air Internal - Mastoid	1	0
Air Internal - Maxillary Sinus	1	0
Air Internal - Oral Cavity	1	0
Air Internal - Sphenoidal Sinus	1	0
Amygdala	69	0.69
Background	1	0
Blood Arteries	48.3	0.537
Blood Veins	48.3	0.537
Brain Gray Matter	60	0.692
Brain White Matter	43.8	0.413
Brainstem Medulla	59.7	0.973
Brainstem Midbrain	59.7	0.973
Brainstem Pons	59.7	0.973

Caudate Nucleus	60	0.692
Cerebellum Gray Matter	52.72	0.942
Cerebellum White Matter	43.8	0.413
Cerebral Peduncles	59.7	0.973
Commissura (Anterior)	43.8	0.413
Commissura (Posterior)	43.8	0.413
Cranial Nerve I - Olfactory	36.9	0.418
Cranial Nerve II - Optic	36.9	0.418
Cranial Nerve III - Oculomotor	36.9	0.418
Cranial Nerve IV - Trochlear	36.9	0.418
Cranial Nerve IX - Glossopharyngeal	36.9	0.418
Cranial Nerve V - Trigeminal	36.9	0.418
Cranial Nerve V2 - Maxillary Division	36.9	0.418
Cranial Nerve V3 - Mandibular Division	36.9	0.418
Cranial Nerve VI - Abducens	36.9	0.418
Cranial Nerve VII - Facial	36.9	0.418
Cranial Nerve VIII - Vestibulocochlear	36.9	0.418
Cranial Nerve X - Vagus	36.9	0.418
Cranial Nerve XI - Accessory	36.9	0.418
Cranial Nerve XII - Hypoglossal	36.9	0.418
CSF General	72.7	2.22
CSF Ventricles	72.73	2.22
Epidermis/Dermis	49.8	0.641
Dura	48	0.804
Ear Auditory Canal	1	0
Ear Auricular Cartilage (Pinna)	46.8	0.553
Ear Cochlea	1	0
Ear Pharyngotympanic Tube	1	0
Ear Semicircular Canals	72.7	2.22
Eye Aqueous	72.7	2.22
Eye Cornea	61.4	1.15
Eye Lens	38.4	0.353
Eye Retina/Choroid/Sclera	60	0.69

Eye Vitreous	69	1.52
Epidermis/Dermis	49.82	0.64
Globus Pallidus	43.8	0.413
Hippocampus	60	0.692
Hyoid Bone	23.2	0.216
Hypophysis or Pituitary Gland	62.4	0.851
Hypothalamus	60	0.692
Intervertebral Discs	47.2	0.911
Mammillary Body	43.8	0.413
Mandible	13.4	0.0827
Mucosa	58.2	0.771
Muscle - Buccinator	58.2	0.771
Muscle - Depressor Anguli Oris	58.2	0.771
Muscle - Depressor Labii	58.2	0.771
Muscle - Inferior Oblique	58.2	0.771
Muscle - Inferior Rectus	58.2	0.771
Muscle - Lateral Pterygoid	58.2	0.771
Muscle - Lateral Rectus	58.2	0.771
Muscle - Levator Labii Superioris	58.2	0.771
Muscle - Levator Scapulae	58.2	0.771
Muscle - Masseter	58.2	0.771
Muscle - Medial Pterygoid	58.2	0.771
Muscle - Medial Rectus	58.2	0.771
Muscle - Mentalis	58.2	0.771
Muscle - Nasalis	58.2	0.771
Muscle - Occipitiofrontalis - Frontal Belly	58.2	0.771
Muscle - Occipitiofrontalis - Occipital Belly	58.2	0.771
Muscle - Orbicularis Oculi	58.2	0.771
Muscle - Orbicularis Oris	58.2	0.771
Muscle - Platysma	58.2	0.771
Muscle - Splenius Capitis	58.2	0.771
Muscle - Sternocleidomastoid	58.2	0.771
Muscle - Superior Oblique	58.2	0.771
Muscle - Superior Rectus	58.2	0.771
Muscle - Trapezius	58.2	0.771

Muscle - Zygomaticus Major	58.2	0.771
Muscle - Zygomaticus Minor	58.2	0.771
Muscle (General)	58.2	0.771
Muscles - Procerus	58.2	0.771
Muscles - Risorius	58.2	0.771
Nasal Septum (Cartilage)	46.8	0.553
Nucleus Accumbens	60	0.692
Optic Chiasm	36.9	0.418
Optic Tract	36.9	0.418
Parotid Gland	78	0.716
Pharynx	1	0
Pineal Body	62.4	0.851
Putamen	60	0.692
Sclera	58.9	0.975
Skull	13.4	0.0872
Skull Diplo	13.4	0.0872
Skull Inner Table	13.4	0.0872
Skull Outer Table	13.4	0.0872
Spinal Cord	36.9	0.418
Subcutaneous Adipose Tissue	11.7	0.0765
Sublingual Gland	78	0.716
Submandibular Gland	78	0.716
Substantia Nigra	59.7	0.973
Teeth	12.454	0.1433
Temporoparietalis	58.2	0.771
Tendon - Galea Aponeurotica	48	0.537
Tendon - Temporalis Tendon	48	0.537
Thalamus	60	0.692
Tongue	58.9	0.745
Vertebra - C1 (atlas)	13.4	0.0827
Vertebra - C2 (axis)	13.4	0.0827
Vertebra - C3	13.4	0.0827
Vertebra - C4	13.4	0.0827
Vertebra - C5	48	13.4

Table A.1.1 | Electromagnetic material parameters composing the MIDA

voxel. Brain tissues are highlighted with yellow shade.

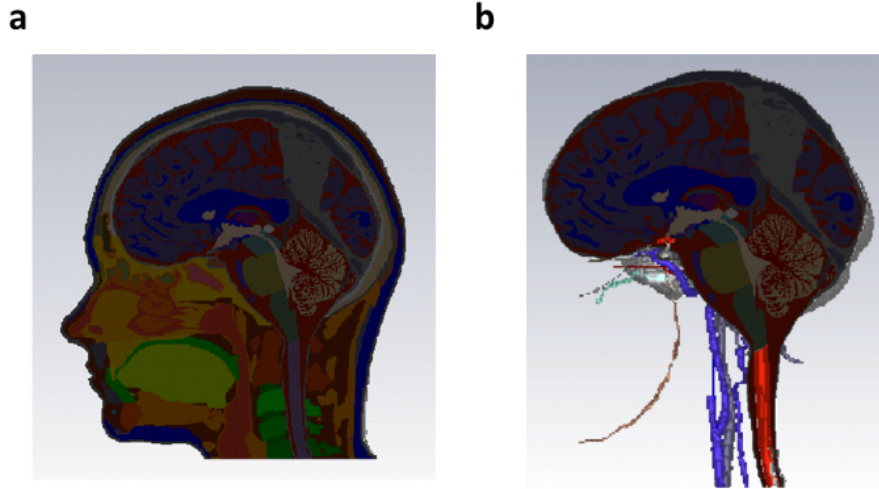


Figure A.1.1 | Sagittal cut of MIDA voxel model for (a) whole head (b) brain.

A.2 Excitation with realistic TEM coils

In order to illustrate the feasibility of the MRI model with coils of idealized current sources, a case with excitation by realistic transverse electromagnetic (TEM) coils is tested. The MRI system with TEM coils consists of 8 elements micro-strip transmission lines that are independently driven, and resonant frequency tuning and impedance matching are performed for each element when the coils are loaded with the human voxel or the mode-shaping pad. Full-wave electromagnetic numerical simulations are carried out using the commercial software Sim4life (ZMT Zurich MedTech AG), which is a representative tool for biomedical simulation. To check the general case, not the trivial case, the voxel with an asymmetric cylindrical pad encircling only half of the ROI is tested. Figure A.2.1 shows B_1^+ field distribution in the sagittal plane for the case under excitation by realistic TEM coils and ideal coils. No significant differences in the field pattern and the mode shaping are observed, especially in the ROI, implying the mode-shaping solutions are compatible with the MRI system using the TEM coils for RF field excitation.

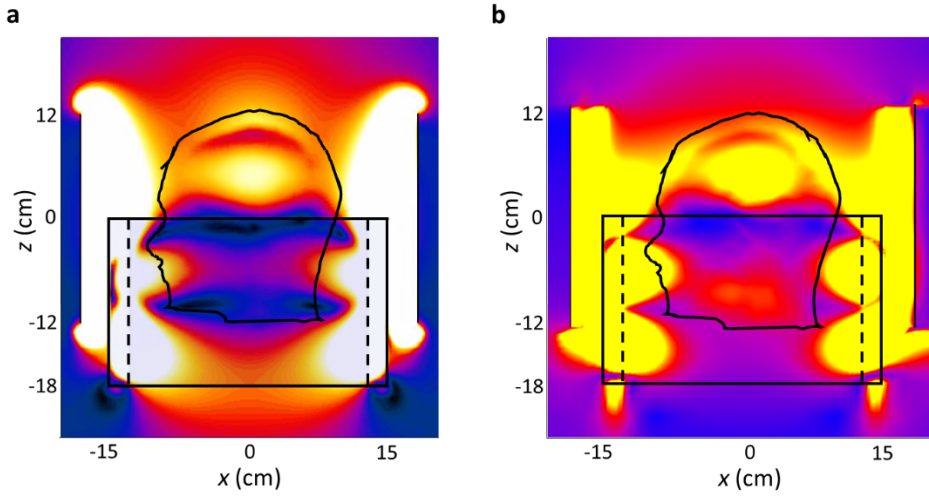


Figure A.2.1 | Comparison of the sagittal images obtained by the MRI system with realistic coils and ideal coils. (a) B_1^+ field distribution in the sagittal plane obtained from MRI system equipped with a realistic eight elements TEM coils. **(b)** Sagittal field profiles in the case of excitation by the MRI RF system with the ideal sources.

Appendix B

Supplements for Chapter 4

B.1 Cylinder can solution for the global homogenization

As mentioned in chapter 4, excitation in the shape of cylindrical symmetry induces improvement of the field homogeneity. It is natural that sharing the shape of a mode gives a similar degree of FOM. Here are examples to show the efficiency of the cylindrical excitation produced by the cylindrical dielectric matching layer.

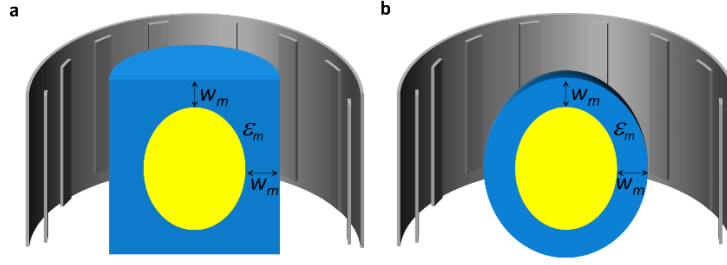


Figure B.1.1 | Schematic of MRI B_1^+ inhomogeneity mitigating system (a) with cylindrical dielectric matching layer and **(b)** with a spheroidal layer. RF coil (gray), spheroidal phantom (yellow), and matching layer (blue) of thickness w_m and electric permittivity ϵ_m .

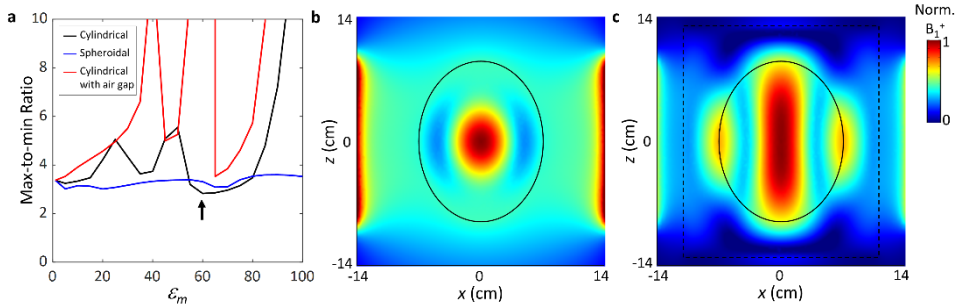


Figure B.1.2 | Effects of the matching layer permittivity ϵ_m and geometry on the GH. (a) B_1^+ Maximum-to-minimum ratio over the phantom with cylindrical layer, spheroidal layer, and the air-gapped-cylinder layer. **(b)** Sagittal ($\theta = 0$) normalized B_1^+ field profiles of the phantom with no matching layer ($\epsilon_m = 1$), and **(c)** with the cylindrical layer of $\epsilon_m = 60$ and $w_m = 4$ cm (point indicated by an arrow in Figure. B.1.2 a). The phantom (solid black ellipse), and the matching layer (black-dashed rectangle).

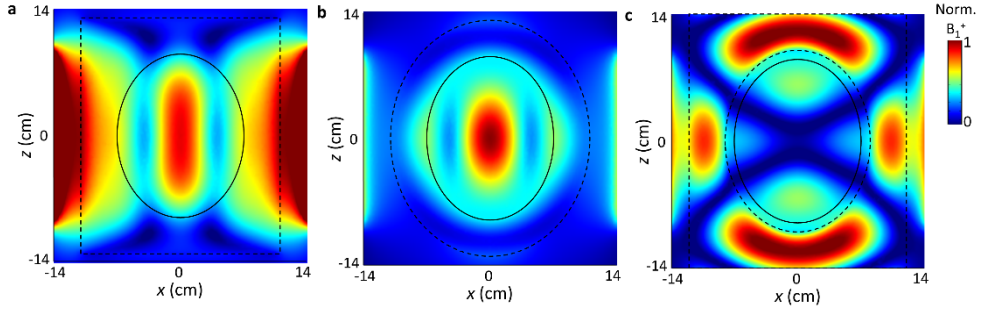


Figure B.1.3 | Mode profiles in the sagittal view for various geometry of the layer: (a) $w_m = 4$ cm cylinder of the phantom material ($\epsilon = 74.2$, $\sigma = 0.87$ S/m), (b) $w_m = 4$ cm spheroid of $\epsilon_m = 60$, and (c) $w_m = 4$ cm cylinder of $\epsilon_m = 60$ with 1 cm air gap between the layer and the phantom.

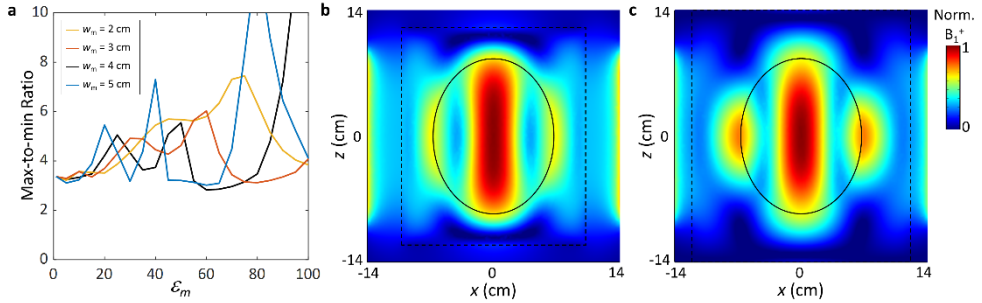


Figure B.1.4 | Effects of the cylindrical layer dimension w_m on the GH over the ROI. (a) Max/min ratio of the phantom with the layer of $w_m = 2$ cm, 3 cm, 4 cm, and 5 cm. (b) Sagittal mode profile of the matched case with the layer of $w_m = 3$ cm, $\epsilon_m = 80$, (c) and with the layer of $w_m = 5$ cm, $\epsilon_m = 50$.

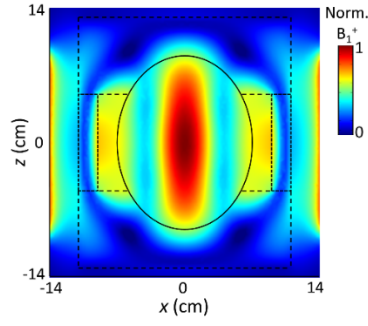


Figure B.1.5 | Mode profile for a matching layer of more realistic geometry. The central part of the $\varepsilon_m = 60$ layer is equivalently replaced with the air-gapped thinner layer of higher index ($w_m = 2$ cm, $\varepsilon_m = 100$), marked with dotted rectangles.

Appendix C

Portions of the work discussed in this dissertation are also presented in the following publications:

M. Park, H. Noh, and N. Park, “Mitigation of B1+ inhomogeneity for ultra-high-field magnetic resonance imaging: hybrid mode shaping with auxiliary EM potential,” Sci. Rep. **10**(1), 1-8 (2020).

Bibliography

- [1] R. Damadian, "Tumor detection by nuclear magnetic resonance," *Science* **171**(3976), 1151-1153 (1971).
- [2] P. Mansfield, and P. K. Grannell, "NMR'diffraction'in solids?," *J. Phys. C* **6**(22), L422 (1973).
- [3] P. C. Lauterbur, "Image formation by induced local interactions: examples employing nuclear magnetic resonance," *Nature* **242**(5394), 190-191 (1973).
- [4] P. C. Lauterbur, "Magnetic resonance zeugmatography," *Pure Appl. Chem.* **40**(1-2), 149-157 (1974).
- [5] K. Ugurbil, R. G. Shulman, and T. R. Brown, "High-resolution ³¹P and ¹³C nuclear magnetic resonance studies of *Escherichia coli* cells in vivo," *Biological Applications of Magnetic Resonance*, 537-589 (Academic Press, 1979).
- [6] R. G. Shulman, T. R. Brown, K. Ugurbil, S. Ogawa, S. M. Cohen, and J. A. Den Hollander, "Cellular applications of ³¹P and ¹³C nuclear magnetic resonance," *Science* **205**(4402), 160-166 (1979).
- [7] P. R. Moran, "A flow velocity zeugmatographic interlace for NMR imaging in humans," *Magn. Reson. Imaging* **1**(4), 197-203 (1982).
- [8] F. W. Smith, J. M. Hutchison, J. R. Mallard, G. Johnson, T. W. Redpath, R. D. Selbie, A. Reid, and C. C. Smith, "Oesophageal carcinoma demonstrated by whole-body nuclear magnetic resonance imaging," *Br Med J (Clin Res Ed)* **282**(6263), 510-512 (1981).
- [9] R. C. Hawkes, G. N. Holland, W. S. Moore, and B. S. Worthington, "Nuclear magnetic resonance (NMR) tomography of the brain: a preliminary clinical assessment with demonstration of pathology," *J. Comput. Assist. Tomogr.* **4**(5), 577-586 (1980).
- [10] R. Y. Kwong, E. K. Yucel, "Computed tomography scan and magnetic resonance imaging," *Circulation* **108**(15), e104-e106 (2003).

- [11] E. C. Ehman, G. B. Johnson, J. E. Villanueva-Meyer, S. Cha, A. P. Leynes, P. E. Z. Larson, and T. A. Hope, "PET/MRI: where might it replace PET/CT?," *J. Magn. Reson. Imaging* **46**(5), 1247-1262 (2017).
- [12] C. H. McDonnell 3rd, R. J. Herfkens, A. M. Norbash, and G. D. Rubin, "Magnetic resonance imaging and measurement of blood flow," *West. J. Med.* **160**(3), 237 (1994).
- [13] M. E. Shenton, C. C. Dickey, M. Frumin, and R. W. McCarley, "A review of MRI findings in schizophrenia," *Schizophrenia research* **49**(1-2), 1-52 (2001).
- [14] F. M. Gunning-Dixon, A. M. Brickman, J. C. Cheng, and G. S. Alexopoulos, "Aging of cerebral white matter: a review of MRI findings," *Int. J. Geriatr. Psychiatry* **24**(2), 109-117 (2009).
- [15] H. Hricak, "MRI of the female pelvis: a review," *Am. J. Roentgenol.* **146**(6), 1115-1122 (1986).
- [16] M. A. Marino, T. Helbich, P. Baltzer, and K. Pinker-Domenig, "Multiparametric MRI of the breast: A review," *J. Magn. Reson. Imaging* **47**(2), 301-315 (2018).
- [17] A. Wadhwa, A. Bhardwaj, and V. S. Verma, "A review on brain tumor segmentation of MRI images," *Magn. Reson. Imaging* **61**, 247-259 (2019).
- [18] I. Ract, J. M. Meadeb, G. Mercy, F. Cueff, J. L. Husson, and R. Guillin, "A review of the value of MRI signs in low back pain," *Diagn. Interv. Imaging* **96**(3), 239-249 (2015).
- [19] G. Constantine, K. Shan, S. D. Flamm, and M. U. Sivananthan, "Role of MRI in clinical cardiology," *The Lancet* **363**(9427), 2162-2171 (2004).
- [20] J. A. Detre, "Clinical applicability of functional MRI," *J. Magn. Reson. Imaging* **23**(6), 808-815 (2006).
- [21] E. Bullmore, "The future of functional MRI in clinical medicine," *Neuroimage* **62**(2), 1267-1271 (2012).
- [22] G. H. Glover, "Overview of functional magnetic resonance imaging," *Neurosurg. Clin. N. Am.* **22**(2), 133-139 (2011).
- [23] S. Ogawa, D. W. Tank, R. Menon, J. M. Ellermann, S. G. Kim, H.

- Merkle, and K. Ugurbil, "Intrinsic signal changes accompanying sensory stimulation: functional brain mapping with magnetic resonance imaging," *Proc. Natl. Acad. Sci.* **89**(13), 5951-5955 (1992).
- [24] E. Zarahn, "Spatial localization and resolution of BOLD fMRI," *Curr. Opin. Neurobiol.* **11**(2), 209-212 (2001).
 - [25] M. R. Zaini, S. C. Strother, J. R. Anderson, J. S. Liow, U. Kjems, C. Tegeler, and S. G. Kim, "Comparison of matched BOLD and FAIR 4.0 T-fMRI with water PET brain volumes," *Med. Phys.* **26**(8), 1559-1567 (1999).
 - [26] M. D. Greicius, G. Srivastava, A. L. Reiss, and V. Menon, "Default-mode network activity distinguishes Alzheimer's disease from healthy aging: evidence from functional MRI," *Proc. Natl. Acad. Sci.* **101**(13), 4637-4642 (2004).
 - [27] J. H. Duyn, "The future of ultra-high field MRI and fMRI for study of the human brain," *Neuroimage* **62**(2), 1241-1248 (2012).
 - [28] D. I. Hoult, and R. E. Richards, "The signal-to-noise ratio of the nuclear magnetic resonance experiment," *J. Magn. Reson.* **24**(1), 71-85 (1976).
 - [29] K. Shmueli, J. A. de Zwart, P. van Gelderen, T. Q. Li, S. J. Dodd, and J. H. Duyn, "Magnetic susceptibility mapping of brain tissue in vivo using MRI phase data," *Magn. Reson. Med.* **62**(6), 1510-1522 (2009).
 - [30] E. Moser, F. Stahlberg, M. E. Ladd, and S. Trattnig, "7-T MR—from research to clinical applications?," *NMR Biomed.* **25**(5), 695-716 (2012).
 - [31] E. Yacoub, A. Shmuel, J. Pfeuffer, P. F. Van De Moortele, G. Adriany, P. Andersen, J. T. Vaughan, H. Merkle, K. Ugurbil, and X. Hu, "Imaging brain function in humans at 7 tesla," *Magn. Reson. Med.* **45**(4), 588-594 (2001).
 - [32] R. Pohmann, O. Speck, and K. Scheffler, "Signal-to-noise ratio and MR tissue parameters in human brain imaging at 3, 7, and 9.4 tesla using current receive coil arrays," *Magn. Reson. Med.* **75**(2), 801-809 (2016).
 - [33] I. Tkáč, G. Öz, G. Adriany, K. Ugurbil, and R. Gruetter, "In vivo ¹H NMR spectroscopy of the human brain at high magnetic fields: metabolite quantification at 4T vs. 7T," *Magn. Reson. Med.* **62**(4), 868-879 (2009).

- [34] M. A. Ertürk, X. Wu, Y. Eryaman, P. F. Van de Moortele, E. J. Auerbach, R. L. Lagore, L. DelaBarre, J. T. Vaughan, K. Uğurbil, G. Adriany, and G. J. Metzger, "Toward imaging the body at 10.5 tesla," *Magn. Reson. Med.* **77**(1), 434-443 (2017).
- [35] B. Guérin, J. F. Villena, A. G. Polimeridis, E. Adalsteinsson, L. Daniel, J. K. White, and L. L. Wald, "The ultimate signal-to-noise ratio in realistic body models," *Magn. Reson. Med.* **78**(5), 1969-1980 (2017).
- [36] F. Lüsebrink, A. Sciarra, H. Mattern, R. Yakupov, and O. Speck, "T 1-weighted in vivo human whole brain MRI dataset with an ultrahigh isotropic resolution of 250 μm ," *Sci. Data* **4**(1), 1-12 (2017).
- [37] W. A. Edelstein, G. H. Glover, C. J. Hardy and R. W. Redington, "The intrinsic signal-to-noise ratio in NMR imaging," *Magn. Reson. Med.* **3**(4), 604-618 (1986).
- [38] B. P. Thomas, E. B. Welch, B. D. Niederhauser, W. O. Whetsell Jr, A. W. Anderson, J. C. Gore, M. J. Avison and J. L. Creasy, "High-resolution 7T MRI of the human hippocampus in vivo," *J. Magn. Reson. Imaging* **28**(5), 1266-1272 (2008).
- [39] K. Kollia, S. Maderwald, N. Putzki, M. Schlamann, J. M. Theysohn, O. Kraff, M. E. Ladd, M. Forsting and I. Wanke, "First clinical study on ultra-high-field MR imaging in patients with multiple sclerosis: comparison of 1.5 T and 7T," *Am. J. Neuroradiol.* **30**(4), 699-702 (2009).
- [40] P. M. L. Robitaille, A. M. Abduljalil, and A. Kangarlu, "Ultra high resolution imaging of the human head at 8 tesla: 2K \times 2K for Y2K," *J. Comput. Assist. Tomogr.* **24**(1), 2-8 (2000).
- [41] S. Gruber, K. Pinker, O. Zaric, L. Minarikova, M. Chmelik, P. Baltzer, R. N. Boubela, T. Helbich, W. Bogner, and S. Trattnig, "Dynamic contrast-enhanced magnetic resonance imaging of breast tumors at 3 and 7 T: a comparison," *Invest. Radiol.* **49**(5), 354-362 (2014).
- [42] R. Krug, C. Stehling, D. A. Kelley, S. Majumdar, and T. M. Link, "Imaging of the musculoskeletal system in vivo using ultra-high field magnetic resonance at 7 T," *Invest. Radiol.* **44**(9), 613-618 (2009).
- [43] S. Trattnig, Š. Zbýň, B. Schmitt, K. Friedrich, V. Juras, P. Szomolanyi, and W. Bogner, "Advanced MR methods at ultra-high field (7 Tesla) for

- clinical musculoskeletal applications,” *Eur. Radiol.* **22**(11), 2338-2346 (2012).
- [44] M. Symms, H. R. Jäger, K. Schmierer, and T. A. Yousry “A review of structural magnetic resonance neuroimaging,” *J. Neurol. Neurosurg. Psychiatry* **75**(9), 1235-1244 (2004).
 - [45] P. M. L. Robitaille, “Ultra high field magnetic resonance imaging: a historical perspective,” *Ultra high field magnetic resonance imaging*, 1-17 (Springer, 2006).
 - [46] K. Uğurbil, “Magnetic resonance imaging at ultrahigh fields,” *IEEE Trans. Biomed. Eng.* **61**(5), 1364-1379 (2014).
 - [47] M. I. Karamat, S. Darvish-Molla, and A. Santos-Diaz, “Opportunities and challenges of 7 tesla magnetic resonance imaging: a review,” *Crit. Rev. Biomed. Eng.* **44**(1-2), 73-89 (2016).
 - [48] E. Moser, “Ultra-high-field magnetic resonance: Why and when?,” *World J. Radiol.* **2**(1), 37-40 (2010).
 - [49] R. R. Regatte, M. E. Schweitzer, “Ultra-high-field MRI of the musculoskeletal system at 7.0 T,” *J. Magn. Reson. Imaging* **25**(2), 262-269 (2007).
 - [50] Y. Duchin, A. Abosch, E. Yacoub, G. Sapiro, and N. Harel, “Feasibility of using ultra-high field (7 T) MRI for clinical surgical targeting,” *PLoS One* **7**(5), e37328 (2012).
 - [51] T. Sinnecker, J. Kuchling, P. Dusek, J. Dörr, T. Niendorf, F. Paul, and J. Wuerfel, “Ultrahigh field MRI in clinical neuroimmunology: a potential contribution to improved diagnostics and personalised disease management,” *EPMA J.* **6**(1), 1-11 (2015).
 - [52] T. Nakada, “Clinical application of high and ultra high-field MRI,” *Brain Dev.* **29**(6), 325-335 (2007).
 - [53] Y. Zhang, J. Z. Cheng, L. Xiang, P. T. Yap, and D. Shen, “Dual-domain cascaded regression for synthesizing 7T from 3T MRI,” *International Conference on Medical Image Computing and Computer-Assisted Intervention*, 410-417 (Springer, 2018).
 - [54] O. Kraff, A. Fischer, A. M. Nagel, C. Mönninghoff, and M. E. Ladd, “MRI at 7 Tesla and above: demonstrated and potential capabilities,” *J.*

- Magn. Reson. Imaging **41**(1), 13-33 (2015).
- [55] F. Schmitt, A. Potthast, B. Stoeckel, C. Triantafyllou, C. J. Wiggins, G. Wiggins, and L. L. Wald, "Aspects of clinical imaging at 7 T," *Ultra High Field Magnetic Resonance Imaging*, 59-103 (Springer, 2006).
 - [56] J. J. Zwanenburg, A. G. van der Kolk, and P. R. Luijten, "Ultra-High-Field MR Imaging: Research Tool or Clinical Need?," *PET Clin.* **8**(3), 311-328 (2013).
 - [57] F. Schick, "Whole-body MRI at high field: technical limits and clinical potential," *Eur. Radiol.* **15**(5), 946-959 (2005).
 - [58] P. Röschmann, "Radiofrequency penetration and absorption in the human body: limitations to high-field whole-body nuclear magnetic resonance imaging," *Med. Phys.* **14**(6), 922-931 (1987).
 - [59] A. Henning, "Proton and multinuclear magnetic resonance spectroscopy in the human brain at ultra-high field strength: a review," *Neuroimage* **168**, 181-198 (2018).
 - [60] M. I. Vargas, P. Martelli, L. Xin, O. Ipek, F. Grouiller, F. Pittau, R. Trampler, R. Gruetter, S. Vulliemoz, and F. Lazeyras, "Clinical neuroimaging using 7 T MRI: challenges and prospects," *J. Neuroimaging* **28**(1), 5-13 (2018).
 - [61] P. Jezzard, and R. S. Balaban, "Correction for geometric distortion in echo planar images from B0 field variations," *Magn. Reson. Med.* **34**(1), 65-73 (1995).
 - [62] P. F. Van de Moortele, C. Akgun, G. Adriany, S. Moeller, J. Ritter, C. M. Collins, M. B. Smith, J. T. Vaughan and K. Ugurbil, "B1 destructive interferences and spatial phase patterns at 7 T with a head transceiver array coil," *Magn. Reson. Med.* **54**(6), 1503-1518 (2005).
 - [63] T. Niendorf, D. K. Sodickson, G. A. Krombach, and J. Schulz-Menger, "Toward cardiovascular MRI at 7 T: clinical needs, technical solutions and research promises," *Eur. Radiol.* **20**(12), 2806-2816 (2010).
 - [64] P. Balchandani, and T. P. Naidich, "Ultra-high-field MR neuroimaging," *AJNR Am. J. Neuroradiol.* **36**(7), 1204-1215 (2015).
 - [65] W. van der Zwaag, A. Schäfer, J. P. Marques, R. Turner, and R. Trampel, "Recent applications of UHF-MRI in the study of human brain function

- and structure: a review,” *NMR Biomed.* **29**(9), 1274-1288 (2016).
- [66] M. E. Ladd, P. Bachert, M. Meyerspeer, E. Moser, A. M. Nagel, D. G. Norris, S. Schmitter, O. Speck, S. Straub, and M. Zaiss, “Pros and cons of ultra-high-field MRI/MRS for human application,” *Prog. Nucl. Magn. Reson. Spectrosc.* **109**, 1-50 (2018).
 - [67] R. H. Caverly, “MRI fundamentals: RF aspects of magnetic resonance imaging (MRI),” *IEEE Microw. Mag.* **16**(6), 20-33 (2015).
 - [68] S. M. Sohn, L. DelaBarre, A. Gopinath, J. T. Vaughan, “RF head coil design with improved RF magnetic near-fields uniformity for magnetic resonance imaging (MRI) systems,” *IEEE Trans. Microw. Theory Techn.* **62**(8), 1784-1789 (2014).
 - [69] T. K. Jhamb, V. Rejathalal, and V. K. Govindan, “A review on image reconstruction through mri k-space data,” *Int. J. Image Graph. Signal Process.* **7**(7), 42-59 (2015).
 - [70] S. C. Lee, “Basic Cardiac Magnetic Resonance Physics for Clinicians-a Clinician's Point of View,” *Int. J. Arrhythm* **17**(3), 135-143 (2016).
 - [71] P. Sprawls, “Nuclear Magnetic Resonance,” *Magnetic Resonance Imaging: Principles, Methods, and Techniques*, 25-34 (Medical Physics Publishing Corporation, 2000).
 - [72] B. E. Saleh, and M. C. Teich, *Fundamentals of photonics*, (John Wiley & sons, 2019).
 - [73] J. T. Vaughan, M. Garwood, C. M. Collins, W. Liu, L. DelaBarre, G. Adriany, P. Andersen, H. Merkle, R. Goebel, M. B. Smith, and K. Ugurbil, “7T vs. 4T: RF power, homogeneity, and signal-to-noise comparison in head images,” *Magn. Reson. Med.* **46**(1), 24-30 (2001).
 - [74] T. S. Ibrahim, R. Lee, A. M. Abduljalil, B. A. Baertlein, P. M. L. Robitaille, “Dielectric resonances and B1 field inhomogeneity in UHFMRI: computational analysis and experimental findings,” *Magn. Reson. Imaging* **19**(2), 219-226 (2001).
 - [75] B. Van Den Bergen, C. A. Van den Berg, L. W. Bartels, J. J. Lagendijk, “7 T body MRI: B1 shimming with simultaneous SAR reduction,” *Phys. Med. Biol.* **52**(17), 5429-5441(2007).
 - [76] A. Laader, K. Beiderwellen, O. Kraff, S. Maderwald, K. Wrede, M. E.

- Ladd, T. C. Lauenstein, M. Forsting, H. H. Quick, K. Nassenstein, and L. Umutlu, "1.5 versus 3 versus 7 Tesla in abdominal MRI: A comparative study," *PloS one*, **12**(11), e0187528 (2017).
- [77] L. L. Wald, and E. Adalsteinsson, "Parallel-excitation techniques for ultra-high-field MRI," *Parallel imaging in clinical MR applications*, 511-521 (Springer, 2007).
 - [78] C. Wang, and G. X. Shen, "B1 field, SAR, and SNR comparisons for birdcage, TEM, and microstrip coils at 7T," *J. Magn. Reson. Med.* **24**(2), 439-443 (2006).
 - [79] J. T. Vaughan, G. Adriany, M. Garwood, E. Yacoub, T. Duong, L. DelaBarre, P. Andersen, and K. Ugurbil, "Detunable transverse electromagnetic (TEM) volume coil for high-field NMR," *Magn. Reson. Med.* **47**(5), 990-1000 (2002).
 - [80] A. Tannús, M. Garwood, "Adiabatic pulses," *NMR Biomed.* **10**(8), 423-434 (1997).
 - [81] M. H. Levitt, and R. Freeman, "NMR population inversion using a composite pulse," *J. Magn. Reson.* **33**(2), 473-476 (1979).
 - [82] Y. Zhu, "Parallel excitation with an array of transmit coils," *Magn. Reson. Med.* **51**(4), 775-784 (2004).
 - [83] W. Grissom, C. Y. Yip, Z. Zhang, V. A. Stenger, J. A. Fessler, and D. C. Noll, "Spatial domain method for the design of RF pulses in multicoil parallel excitation," *Magn. Reson. Med.* **56**(3), 620-629 (2006).
 - [84] FDA 510(k) premarket approval under No. K170840 for Magnetom Terra 7 T, Oct. 2017.
 - [85] Q. X. Yang, W. Mao, J. Wang, M. B. Smith, H. Lei, X. Zhang, K. Ugurbil, and W. Chen, "Manipulation of image intensity distribution at 7.0 T: passive RF shimming and focusing with dielectric materials," *J. Magn. Reson. Imaging* **24**(1), 197-202 (2006).
 - [86] K. Haines, N. B. Smith, and A. G. Webb, "New high dielectric constant materials for tailoring the B1+ distribution at high magnetic fields," *J. Magn. Reson.* **203**(2), 323-327 (2010).
 - [87] W. M. Teeuwisse, W. M. Brink, and A. G. Webb, "Quantitative assessment of the effects of high-permittivity pads in 7 Tesla MRI of

- the brain,” *Magn. Reson. Med.* **67**(5), 1285-1293 (2012).
- [88] W. M. Teeuwisse, W. M. Brink, K. N. Haines, and A. G. Webb, “Simulations of high permittivity materials for 7 T neuroimaging and evaluation of a new barium titanate-based dielectric,” *Magn. Reson. Med.* **67**(4), 912-918 (2012).
 - [89] A. L. Neves, L. Leroi, Z. Raolison, N. Cochinaire, T. Letertre, R. Abdeddaïm, S. Enoch, J. Wenger, J. Berthelot, A.-L. Adenot-Engelvin, N. Malléjac, F. Mauconduit, A. Vignaud, and P. Sabouroux, “Compressed perovskite aqueous mixtures near their phase transitions show very high permittivities: New prospects for high-field MRI dielectric shimming,” *Magn. Reson. Med* **79**(3), 1753-1765 (2018).
 - [90] T. P. A. O’Reilly, A. G. Webb, and W. M. Brink, “Practical improvements in the design of high permittivity pads for dielectric shimming in neuroimaging at 7 T,” *J. Magn. Reson.* **270**, 108-114 (2016).
 - [91] W. M. Brink, A. M. van der Jagt, M. J. Versluis, B. M. Verbist, and A. G. Webb, “High permittivity dielectric pads improve high spatial resolution magnetic resonance imaging of the inner ear at 7 T,” *Invest. Radiol.* **49**(5), 271-277 (2014).
 - [92] R. Schmidt, A. Slobozhanyuk, P. Belov, and A. Webb, “Flexible and compact hybrid metasurfaces for enhanced ultra high field in vivo magnetic resonance imaging,” *Sci. Rep.* **7**(1), 1-7 (2017).
 - [93] M. Dubois, L. Leroi, Z. Raolison, R. Abdeddaim, T. Antonakakis, J. De Rosny, A. Vignaud, P. Sabouroux, E. Georget, B. Larrat, G. Tayeb, N. Bonod, A. Amadon, F. Mauconduit, C. Poupon, D. Le Bihan, and S. Enoch “Kerker effect in ultrahigh-field magnetic resonance imaging,” *Phys. Rev. X.* **8**(3), 031083 (2018).
 - [94] J. H. F. van Gemert, W. M. Brink, A. G. Webb, and R. F. Remis, “High-Permittivity Pad Design for Dielectric Shimming in Magnetic Resonance Imaging Using Projection-Based Model Reduction and a Nonlinear Optimization Scheme,” *IEEE Trans. Med. Imaging* **37**(4), 1035-1044 (2018).
 - [95] J. van Gemert, W. Brink, A. Webb, and R. Remis, “High-permittivity pad design tool for 7T neuroimaging and 3T body imaging,” *Magn. Reson. Med.* **81**(5), 3370-3378 (2019).

- [96] S. Jensen, "The nonlinear coherent coupler," *IEEE J. Quantum Electron.* **18**(10), 1580-1583 (1982).
- [97] K. Y. Bliokh, F. J. Rodríguez-Fortuño, F. Nori, and A. V. Zayats, "Spin-orbit interactions of light," *Nat. Photonics* **9**(12), 796-808 (2015).
- [98] K. M. Gundu, M. Kolesik, J. V. Moloney, "Mode shaping in multicore fibers," *Opt. Lett.* **32**(7), 763-765 (2007).
- [99] A. Mafi, and J. V. Moloney, "Shaping modes in multicore photonic crystal fibers," *IEEE Photon. Technol. Lett* **17**(2), 348-350 (2005).
- [100] S. Kawakami, and S. Nishida, "Characteristics of a doubly clad optical fiber with a low-index inner cladding," *IEEE J. Quantum Electron.* **10**(12), 879-887 (1974).
- [101] S. Kawakami, and S. Nishida, "Perturbation theory of a doubly clad optical fiber with a low-index inner cladding," *IEEE J. Quantum Electron.* **11**(4), 130-138 (1975).
- [102] T. P. Tanaka, S. I. Onoda, and M. Sumi, "W-type optical fiber: relation between refractive index difference and transmission bandwidth," *Appl. Opt.* **15**(5), 1121-1122 (1976).
- [103] P. K. Tien, "Rules of refractive index and a potential well model of the optical waveguides," *Radio Sci.* **16**(4), 437-444 (1981).
- [104] P. K. Tien, "Integrated optics and new wave phenomena in optical waveguides," *Rev. Mod. Phys.* **49**(2), 361-420 (1977).
- [105] T. K. Foo, C. E. Hayes, and Y. W. Kang, "An analytical model for the design of RF resonators for MR body imaging," *Magn. Reson. Med.* **21**(2), 165-177 (1991).
- [106] T. K. Foo, C. E. Hayes, and Y. W. Kang, "Reduction of RF penetration effects in high field imaging," *Magn. Reson. Med.* **23**(2), 287-301 (1992).
- [107] A. G. Webb, "Dielectric materials in magnetic resonance," *Concept. Magn. Reson. A* **38**(4), 148-184 (2011).
- [108] W. M. Brink, R. F. Remis, and A. G. Webb, "A theoretical approach based on electromagnetic scattering for analysing dielectric shimming in high-field MRI," *Magn. Reson. Med.* **75**(5), 2185-2194 (2016).

- [109] R. Schmidt, and A. Webb, "Improvements in RF shimming in high field MRI using high permittivity materials with low order pre-fractal geometries," *IEEE Trans. Med. Imaging* **35**(8), 1837-1844 (2016).
- [110] M. V. Vaidya, M. Lazar, C. M. Deniz, G. G. Haemer, G. Chen, M. Bruno, D. K. Sodickson, R. Lattanzi, and C. M. Collins, "Improved detection of fMRI activation in the cerebellum at 7T with dielectric pads extending the imaging region of a commercial head coil," *J. Magn. Reson. Imaging* **48**(2), 431-440 (2018).
- [111] C. M. Collins, S. Li, M. B. Smith, "SAR and B1 field distributions in a heterogeneous human head model within a birdcage coil," *Magn. Reson. Med.* **40**(6), 847-856 (1998).
- [112] Food and Drug Administration. Criteria for significant risk investigations of magnetic resonance diagnostic devices - Guidance for Industry and Food and Drug Administration Staff. June 13, 2014. Available at: [https://www.fda.gov/downloads/medicaldevices/device regulationandguidance/guidancedocuments/ucm072688.pdf](https://www.fda.gov/downloads/medicaldevices/device%20regulationandguidance/guidancedocuments/ucm072688.pdf). Accessed December, 2020.
- [113] International Electrotechnical Commission. Medical electrical equipment - Part 2-33: Particular requirements for the basic safety and essential performance of magnetic resonance equipment for medical diagnosis. IEC 60601-2-33 ed30 2010. Available at: <https://webstore.iec.ch/publication/2647>. Accessed December, 2020.

국문 초록

자기 공명 영상법은 안정성과 확장성을 바탕으로 가장 광범위하게 이용되고 있는 영상 기법 중 하나이다. 자기 공명 영상법은 동작 정 자기장을 높임으로써 영상의 질을 향상시킬 수 있는데, 최근에는 7T 이상의 초고자장 자기 공명 영상법이 활용되고 있다. 초고자장 자기 공명 영상법은 신호 대비 잡음도, 공간 시간 해상도, 대조도 등을 향상시키는데, 이를 통해 특히 뇌 정밀 영상 촬영에 대체 불가능한 강점을 가진다. 이러한 장점에도 불구하고 정 자기장의 증가는 고주파 신호 B_1^+ 필드의 불균일성을 야기하며, 이는 다시 이미지 품질을 떨어뜨리는 등 원치 않는 영향으로 이어진다.

B_1^+ 필드 불균일성 문제를 해결하기 위해 다양한 방법이 시도되었으며, 이 중에서도 유전체 물질로 채운 구조물인 패드를 이용한 수동 보정 접근은 기존 시스템에 호환이 되고 안정성을 인정받아 임상에서의 적용 가능성이 알려져 있는 대표적인 전략이다. 필드 패턴을 바꾸어주는 효과를 기반으로 하여 관심 영역에 붙여 주변부의 불균일성을 성공적으로 완화하는 이 방법은 최근 고 유전체 물질의 활용과 더불어 관심을 받고 있지만, 관심 부분 영역 전체에 대해서는 악영향을 수반하므로 광역 균일화를 위한 방법에 대한 연구가 필요하다.

본 학위 논문에서는, B_1^+ 필드의 광역 균일화를 위한 방법으로 퍼텐셜의 에바네센트 커플링을 기반으로 한 모드 성형 방식을 제안한다.

인체를 공진기로 보고 그것과 에바네센트 결합을 하는 보조 퍼텐셜을 적용함으로써 모드 성형 능력을 확인하였으며, 그것을 조절함으로써 스캐닝하려는 대상의 형태나 물질 분포에 강건한 축성 B_1^+ 필드의 광역 균일화를 구현할 수 있다. 또한, 해당 개념을 확장하여 삼차원 광역 균일화를 수행하는 모드 성형법을 제안한다. 이와 더불어, 이러한 모드 성형법의 실제적 적용가능성을 평가하기 위해 SAR와 강건성 분석을 수행하였다. 본 연구는 초고자장 자기 공명 영상법의 B_1^+ 불균일성 완화에 대한 색다른 시각과 체계적인 방법을 제공함으로써 고주파 신호 균일화에의 수동 보정 방법의 역할을 확장하는 지침이 될 것으로 기대된다.

주요어 : 초고자장 자기 공명 영상법, 고주파 B_1^+ 불균일성, 고주파 수동 보정, 모드 성형, 보조 전자기 퍼텐셜

학번 : 2013-20790